

CHARLES UNIVERSITY IN PRAGUE
FACULTY OF MATHEMATICS AND PHYSICS
DEPARTMENT OF ELECTRONICS AND VACUUM PHYSICS



THESIS

Early stages of indium growth
on the Si(100) surface

Jakub Javorský

Supervisor: Ivan Ošťádal
Consultant: Pavel Sobotík

There are many people that provided advice, guidance and support during my work on this thesis. My thanks belong particularly to Ivan Ošťádal, Pavel Sobotík and Pavel Kocán who shared with me their knowledge of physics, electronics, fine mechanics and navigation through the perils of scientific diplomacy.

I am indebted to thank Miroslav Kotrla from Academy of Sciences of the Czech Republic, who advised me on programming and analysis of the simulations forming part of the work.

Finally, I must mention my fellow Ph.D. student Martin Setvín, who participated in many experiments and discussions related to this thesis.

Overview

We start this work by introducing the reader to the Si(100) surface and various processes that are known or could be expected to occur on the surface when depositing very small amounts of indium (a group III metal). Then we briefly describe several theoretical and simulation-based approaches suitable to study of the In/Si(100) system and finally we describe the scanning tunneling microscopy and its applicability. We will present the atomic structure of indium chains that spontaneously form on the surface, identify main processes that guide the growth and evolution of the chains, determine diffusion barriers of single In atoms and study the decay of the In chains. Our results are presented in form of three published articles, commented with respect to evolution of our knowledge and other group's results, and recent findings from the low temperature experiments.

Contents

| | | |
|----------|--|-----------|
| 1 | Atomic processes on surfaces | 6 |
| 1.1 | Kinetic approach | 6 |
| 1.1.1 | Deposition, adsorption sites, desorption | 7 |
| 1.1.2 | Diffusion | 8 |
| 1.1.3 | Nucleation and rate equations | 9 |
| 1.2 | Role of defects | 10 |
| 1.3 | Scaled island-size distribution | 10 |
| 1.4 | Ab-initio calculations for surface physics | 13 |
| 2 | Monte Carlo simulations of growth | 13 |
| 2.1 | Kinetic Monte Carlo | 14 |
| 2.2 | Comments on the algorithm | 15 |
| 2.3 | KMC and other methods | 15 |
| 3 | The STM technique | 17 |
| 3.1 | Principles | 17 |
| 3.2 | Implementation | 19 |
| 3.3 | STS and LDOS maps | 20 |
| 3.4 | Variable temperature STM | 20 |
| 3.5 | Real-time STM observations | 22 |
| 3.6 | Diffusion measurements | 23 |
| 3.7 | The STM tip | 23 |
| 4 | Metals on Si(100)-2×1 | 27 |
| 4.1 | Introduction | 27 |
| 4.2 | The Si(100) surface | 27 |
| 4.3 | Defects on the Si(100) | 30 |
| 4.4 | Group III and IV metals on Si(100) | 30 |
| 4.5 | Group III metals | 31 |
| 4.6 | Group IV metals | 32 |
| 4.7 | Coadsorption of Group III and IV metals | 33 |
| 5 | Experimental Setup | 34 |
| 5.1 | Ultra-high Vacuum Chamber - KFPP | 34 |
| 5.2 | STM head | 35 |
| 5.3 | Ultra-high Vacuum Chamber - FZU AV | 35 |
| 5.4 | Sample treatment | 37 |

| | | |
|----------|--|-----------|
| 5.5 | Deposition | 39 |
| 6 | In chains on Si(100)-2×1 | 40 |
| 6.1 | In at room temperature | 40 |
| 6.2 | In chain structure | 40 |
| 6.3 | In chain evolution | 42 |
| 6.4 | Tip influence (Publication 1 - Kocan 2007) | 50 |
| 6.5 | Detachment energies | 56 |
| 6.6 | Kinetics of In growth (Publication 2 - Ostadal 2008) | 59 |
| 6.7 | Diffusion of In (Publication 3 - Javorsky 2009) | 64 |
| 6.8 | Low temperature observation of In on Si(100) | 75 |
| 7 | Summary | 79 |

1 Atomic processes on surfaces

This section brings overview of the initial stage of thin film growth on crystal surfaces (epitaxial growth) and explains the terms used throughout the thesis.

This work focuses only on very early stages of growth, well below the first atomic monolayer (ML).

1.1 Kinetic approach

Kinetic approach describes the time evolution of processes during the growth - arriving deposited atoms on surface, adsorption and diffusion over the surface. The surface, along with steps, imperfections and adsorbed atoms determines the shape of the so called surface potential. The set of points of the surface potential with the same energy describes the Potential Energy Surface (PES). Atoms adsorbed on the surface dwell in more or less stable positions in minima of this potential. From the kinetic point of view, to get from one such minimum to another, the particle must overcome a potential barrier. The frequency with which the particle moves from one position to another is a function of surface temperature. In fact, all surface processes, with the exception of deposition, can be described as thermally activated. From the transition state theory [1], the rates of thermally activated processes can be expressed as:

$$h = \nu_0 \exp[-E_{act}/(k_B T)] \quad (1)$$

where T is temperature, ν_0 is attempt frequency and E_{act} is activation energy, k_B is the Boltzmann constant. A growth model can be developed using the most frequent processes. The most common processes include:

- Deposition - Atoms are deposited on the surface. An atom hitting the surface needs not necessarily be permanently trapped on the surface. It may bounce off the surface or make a bond and desorb later.
- Desorption - Adatoms can leave the surface. The probability of an adatom leaving the surface depends on its bond with the substrate (represented by the adsorption energy) and surface temperature. Desorption may be neglected if the surface temperature is sufficiently low.
- Diffusion - Atoms may generally migrate along the surface or even penetrate into the substrate.

- Growth of islands - migrating adatoms become trapped at sites with higher bonding energy (surface defects, step edges, impurities) or make a bond with other adatom. Initial nuclei then either decay or grow larger into stable islands.
- Coalescence - growing islands have no more lateral space (the average diameter of islands becomes of the same order as the distance of its centers), two touching islands create one larger and the density of islands decreases. During this process the islands can either change drastically their shapes or stay almost unchanged.

These processes depend on the combination of materials of substrate and adsorbate, on the crystallographic plane of the substrate and on substrate reconstruction. Surface morphology determines adsorption sites and, if anisotropic, may cause anisotropic diffusion and island formation.

1.1.1 Deposition, adsorption sites, desorption

Many methods exist for deposition of material on surface, e.g. thermal evaporation, sputtering and ion beam assisted techniques, molecular beam epitaxy (MBE), chemical vapour deposition (CVD) techniques, electroplating, anodizing and many more. STM is usually used to study films grown in ultra-high vacuum condition (UHV). Such very low pressure make it possible to observe clean surfaces or the adatom layer as-prepared, before it is contaminated. It is also possible to observe clean surfaces before deposition of the studied material and then compare with images of grown layer. Vacuum deposition methods, usually MBE, thermal or electron-beam evaporation techniques, are used in combination with STM, because the deposition rate can be well defined and controlled. Deposited atoms are not immediately thermalized to surface temperature. Even at temperatures when all diffusion should be stopped, islands are known to form, indicating the atoms have migrated at least a limited distance. The incoming atoms have excess kinetic energy, which is gradually lost by interactions with the substrate. Before the atom loses this extra energy and gets to thermal equilibrium with the substrate, it hops along the surface. Especially high-energy impacting particles, as is the case of electron beam evaporators (where the material is heated by an electron beam) which also charge and accelerate the particles are known to jump 2-10 times before accommodating [2].

Atoms are transported from the source to random positions on the surface and relax to the bottom of the nearest potential well in thermal equilibrium with the substrate. Such positions are called adsorption sites. The depth of the potential

minimum is called adsorption energy E_{ads} . E_{ads} is negative because it expresses the energy the atom lost during adsorption. The arrival rate of atoms or molecules to surface depends on the deposition source temperature, system geometry, pressure and type of atoms or molecules. Desorption is a thermally activated process and it also depends on the strength of the bond between adatoms, adsorption position and on coverage.

1.1.2 Diffusion

Thermal fluctuations may temporarily provide an adatom with energy to escape from its potential well. This energy is usually not enough for desorption (typically 1 to 5 eV), but may suffice to move to a neighboring adsorption position. In case of an atom on a periodic 2D lattice of adsorption sites, this movement (hopping) can be described as a random walk, since each jump is uncorrelated to the previous one. Then, the tracer diffusion coefficient D can be expressed using the Einstein's formula as:

$$D = \frac{1}{4t} \langle |\Delta \mathbf{r}|^2 \rangle, \quad (2)$$

where $\Delta \mathbf{r}$ is total displacement of the atom after time t .

Diffusion can be considered as a thermally activated process described by the equation 1. For square, hexagonal or triangular lattices, the diffusion coefficient D can be expressed as

$$D = \frac{1}{4} a^2 \nu, \quad (3)$$

where a is the distance between adsorption sites and ν is the frequency of jumps. For anisotropic lattices, the diffusion coefficient is anisotropic.

Using eq. 1 and eq. 3 we then get the following relation between the diffusion coefficient and diffusion barriers E_D :

$$D = D_0 \exp\left(-\frac{E_D}{kT}\right), \quad (4)$$

where

$$D_0 = \frac{\nu_0 a^2}{4}. \quad (5)$$

In the vicinity of step edges, kinks, surface imperfections and near other adatoms, the hopping probability is different. This is caused by a different number of bonds the adatom has with the surface and/ or other adatoms and different depth of potential wells around surface imperfections. Binding energy is usually

higher at lower step edges, leading to diffusion along steps and, in homoepitaxy, to the so called step flow mode of growth, in which a new atomic layer is formed by attaching atoms to lower step edge. On the other hand, diffusion from the upper terrace down is often blocked by a potential barrier due to lower number of neighboring atoms at the position on the top of the step [3].

1.1.3 Nucleation and rate equations

The migrating adatoms find eventually another adatom, create an adatom-adatom bond and thus form a nuclei of an island. Islands are not necessarily stable - they evolve in both size and shape. Time evolution of island concentration can be described with rate equations: a set of differential equations encompassing all important atomic scale processes and long-range interactions. Solving the set of equations provides dynamical evolution of island size distribution $n_i(\Theta)$ defined as a number of islands per unit area containing i atoms (at coverage Θ). The method is often combined with Kinetic Monte Carlo simulations.

In [4], Venables solves the problem using following presumptions:

1. Only single atoms are mobile on the surface.
2. Low coverage is considered.
3. We can define a critical cluster size i . Islands above this size are stable, meaning on average another adatom arrives to the cluster before an atom detaches from it; the reverse is valid for clusters below this size. Concentration of stable islands is n_x .
4. Subcritical-size clusters are in local equilibrium with adatom population.
5. Desorption is negligible.

Then, we can write:

$$dn_1/dt = R\sigma_i D n_1 n_i - \sigma_x D n_1 n_x \quad (6)$$

$$dn_j/dt = 0 \text{ (for } 2 \leq j \leq i) \quad (7)$$

$$dn_x/dt = \sigma_i D n_1 n_i - U_{coal} \quad (8)$$

$$n_j = (n_1)^j \sum_m C_j(m) \exp\left(\frac{E_j(m)}{kT}\right) \quad (9)$$

where R is flux of atoms, σ_i is a so called "capture number" describing average island geometry, D is the tracer diffusion coefficient, U_{coal} is the decrease of critical islands due coalescence, $C_j(m)$ is the statistical weight of islands size j and configuration m . Equation 6 describes the change of free adatom concentration due deposition and capture by clusters. Eq. 7 represents local equilibrium of subcritical-size island population, eq. 8 change of concentration of stable islands, eq. 9 is the well known Walton relation. By solving this set of equations, we get:

$$n_x \approx \left(\frac{D}{R}\right)^{-x} \exp\left(\frac{E_j}{kT}\right) \quad (10)$$

$$\chi_{2D} = \frac{i}{i+2} \quad E = \frac{E_i + iE_D}{i+2} \quad (11)$$

$$\chi_{3D} = \frac{i}{i+2,5} \quad E = \frac{E_i + iE_D}{i+2,5}. \quad (12)$$

STM enables to measure island density at such temperatures when $i = 0$. Then $E_i = 0$ and it is possible to obtain the value of diffusion barrier E_D . With known E_D and i , it is then possible to measure the effective binding energy E_i . However, no information about the shape of the islands is gained.

1.2 Role of defects

Imperfections in surface lattice and presence of adsorbed contamination can affect growth of a film. These sites may act as nucleation centers. In systems with high adsorbate diffusion, such sites may strongly affect island density. On the other hand, defects may trap migrating adatoms, effectively inhibiting diffusion. This affects growth especially in systems with highly anisotropic diffusion. The exact influence of Si(100) surface defects on indium (and other group III metals) is studied and discussed in section Results.

1.3 Scaled island-size distribution

We need to describe the grown layers in such a means that would allow us to compare general properties of a layer as a whole with other layers, be it the same combination of materials prepared under different conditions, or different combination of materials. Commonly used quantities used to describe statistical parameters of a layer include the mean island size, concentration of islands and island-size distribution function. While the terms "mean island size" and "concentration of islands" are quite self-explanatory, let us focus on the island-size

distribution function in more detail. In this section, we shall briefly explain the term and discuss some commonly observed shapes of the island-size distribution function.

From the nucleation theory [5] it follows that the density per site N_s of islands composed of s atoms can be expressed as:

$$N_s \approx \frac{\Theta}{\langle s \rangle^2} f(s/\langle s \rangle) \quad (13)$$

where Θ denotes coverage, and $\Theta/\langle s \rangle$ denotes the mean island size density. The function $f(x)$, $x = s/\langle s \rangle$ is the scaled island size distribution function (a normalized histogram of island size). The normalization is set to fulfill the relations:

$$\int_{x \geq 0} f(x) dx = \int_{x \geq 0} x f(x) dx = 1 \quad (14)$$

The shape of the function can be analytically derived from solving the rate equations. Bartelt and Evans [5, 6] solved the equations for *irreversible* growth (no atom detachment from islands), considering the islands as sizeless sinks. Then, the island size distribution function is monomodal with a peak around $x = 1$ (Fig. 1). The peak becomes sharper and higher with increasing D/F ratio (diffusion rate/ incoming flux). Ratsch et. al. derived the island-size distribution function also for reversible growth [7] and showed that the width of the peak also decreases with higher critical size i , above which islands are stable.

Tokar [8] derived the island-size distribution for the thermodynamic equilibrium state using a 1-D and 2-D model with nearest-neighbour interatomic interaction. Detachment from islands is permitted in this model, quantified by a constant nearest-neighbour interaction energy. The dependence on diffusion rate is irrelevant, since the model is valid for equilibrium. In this model, the island size distribution function is exponentially decreasing - see Fig. 2.

Note that thanks to the normalized state of the distribution function, the shape of the function is similar for various coverages, as long as the presumptions considered for deriving the distribution functions are met. Parameters such as diffusion barriers, deposition rates, detachment rates etc. are introduced into the scaled island-size distribution through the rate equations. As a consequence, island size distributions can be simulated and compared to experimentally measured functions to obtain these parameters. However, if the observed system has reached or is close to thermodynamical equilibrium, no kinetic parameters (such as diffusion barriers) can be obtained, because in equilibrium the function no longer depends on kinetic parameters. We should also note that most analytical solutions for the

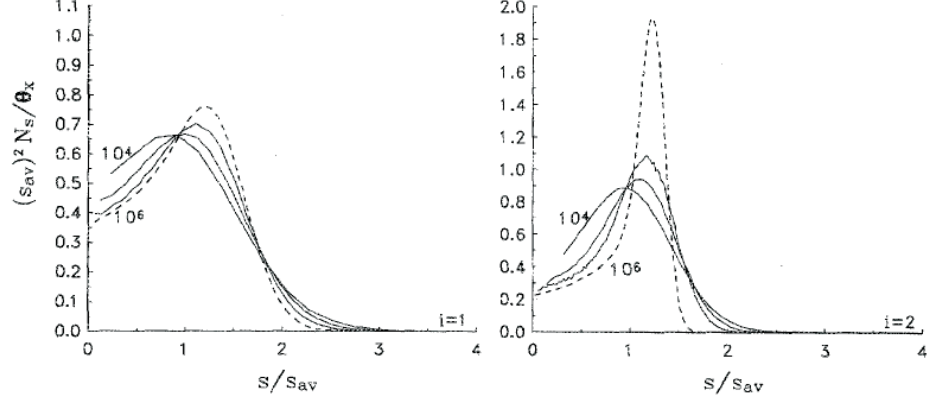


Figure 1: Examples of a monomodal shape of the distribution function taken from [6]. Monomodal shape is typical for both 1-D and 2-D growth with no detachment from islands. Plotted for critical island size=1 (left) and 2 (right), isotropic diffusion. Individual curves show different D/F ratios.

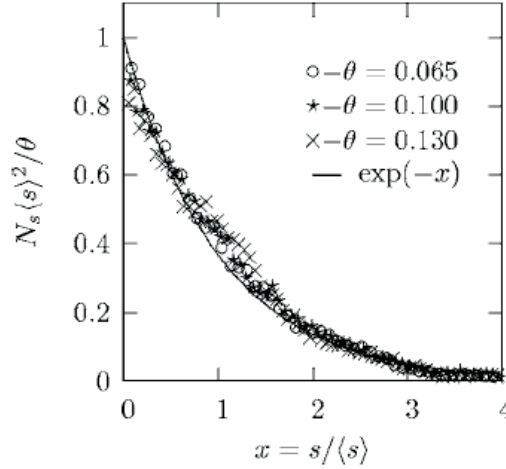


Figure 2: Examples of an exponentially decreasing distribution function taken from [8]. Exponentially decreasing function was derived on a basis of only nearest-neighbour interactions in an island, for a system in equilibrium. The dots represent data from [9], the line is the derived theoretical curve fitted to these data.

scaled island-size distribution function are valid only for low coverage (up to ≈ 0.1 ML), due to the deriving presumptions.

1.4 Ab-initio calculations for surface physics

On the basis of a set of fundamental physical laws, ab-initio calculations determine adsorption positions of adsorbed atoms and/or changes to the substrate structure by searching for system configuration with minimum energy. For modeling semiconductor surfaces, electrons are treated using quantum mechanics, while ions classically. Only some atoms are allowed to change positions, others are fixed at known positions (bulk atoms). Such calculations are extremely time-consuming and even though many methods and approximations have been developed, only small systems can be studied this way.

A very common method used is the Density Functional Theory - DFT [10]. It is based on the presumption that one can find the ground energy of a many-body system as a unique functional of the ground state charge density. The potential of atomic nuclei and electrons is approximated by an effective potential that is only a function of three spatial coordinates. Thus, the number of variables in the calculation is greatly reduced. The exchange-correlation energy density of the *inhomogeneous* electron distribution is often replaced by the exchange-correlation energy density of *homogeneous* electron gas. This is called Local Density Approximation(LDA) [11].

Another common method is the molecular dynamics. In molecular dynamics, positions of atoms are changed in very small time steps (10^{-12} s) as determined by solving Newton equations. This method is useful to study time evolution of small clusters (modeling catalytic reactions, growth or decay of small islands). Due to the small time step, it is not suitable to study processes encompassing many particles and longer time scales (such as deposition, overall growth of a layer etc.).

2 Monte Carlo simulations of growth

One method of studying thin film layers and testing models thereof is the use of computer simulation. Simulations enable us to visualize processes and thin film layer details not accessible via experimental means or predict thin film properties, which can be then compared with experimental results. Monte Carlo (MC) is a class of simulations that rely on repeated random sampling to compute their results. Monte Carlo methods are most suitable for simulating tasks involving large number of degrees of freedom (fluids, disordered materials), modeling phenomena that involve random events (particle physics, economy) and for computing

multi-dimensional definite integrals. Regarding thin film growth, Monte Carlo was originally used to find minimum energy by introducing random changes of the system. No kinetic phenomena were included.

2.1 Kinetic Monte Carlo

To simulate time evolution of some processes, Monte Carlo can be modified to include random events occurring at random moments. Since it is extremely difficult to precisely describe processes like desorption of atoms, atom hopping to neighbouring site etc., we can instead describe the process as random events that occur with a certain rate. In surface physics, this rate is the rate of thermally activated processes (see Section 1). Then we can simulate growth and evolution of layer of adatoms by generating random events given by the rates. A physical model must be prepared, which contains one or more parameters controlling the event rates (for example, the diffusion barrier height). The parameter is then fitted so that the simulation results match the observations (experimental data).

In thin film simulations, there are two types of Kinetic Monte Carlo (KMC) simulation events:

1. Events simulating a thermally activated process. Each such process is described by its activation energy (eq. 1) and all depend on an external parameter - temperature.
2. Events not thermally activated. Their rates are determined by outer factors. An example could be deposition of adatoms on the surface.

Details of the physical model and possible events used in this work are described in Publication 3 in section 6.7.

In the basic KMC algorithm, a constant time step Δt is selected. At each step, probability p of each of N possible realization is calculated using formula:

$$p_i = 1 - \exp(-r_i \Delta t), \quad (15)$$

where r_i is the rate of the event i . The time step must be selected sufficiently low not to skip any high-rate event. Therefore, this algorithm is very time consuming.

Nowadays, a faster Bortz-type algorithm [12] is almost exclusively used for modelling surface processes and is also used in this work. There is no definite time step. Instead, time between individual random events is calculated. In each simulation step, cumulative rates R_j are calculated:

$$R_j = \sum_{i=1}^j r_i \quad , \quad j = 1, 2, \dots, N \quad (16)$$

Then, a random number $a \in (0,1)$ is generated with uniform distribution. Using equation:

$$\Delta t = \frac{-\ln(a)}{R_N}, \quad (17)$$

the time step to the next event is selected. The type of an event is determined by generating another random number with uniform distribution - $b \in (0,1)$. The event for which $R_{j-1} < bR_N \leq R_j$ will be realized. Thus, probability of selection of an event is proportional to its rate. One can imagine this algorithm as having a line of a length R_N divided into intervals i , whose length corresponds to probability of realization of the event. One event is selected by randomly pointing at one of the intervals.

2.2 Comments on the algorithm

If the processes associated with rates i are independent (not correlated) Poisson type, as can be presumed for thermally activated surface processes, this algorithm provides correct time scale for system evolution. Compared to the basic KMC, the The Bortz-type algorithm produces an event in each time step. The most time-consuming is the selection of the next event. By dividing the events into groups, subgroups etc. and random searching within this structure, the efficiency can be optimized from N to \sqrt{N} . Details of the implementation can be found for example in [12, 13, 14]. Bortz-type algorithm considers rates as fixed. Should the rates change during the simulation (i.e. by change of temperature, by depositing new adatoms on the surface etc.), the rates must be re-calculated. Generally, rates are re-calculated before each step in KMC simulations used in this work.

2.3 KMC and other methods

KMC can be used in combination with ab-initio calculations to simulate layer growth (time scale in the range of seconds) with respect to individual events (nanosecond time scale). Activation energies should be calculated in each step instead of using a pre-defined values. Such approach is too computationally exhaustive even for today's computers, so a less precise approach is adopted - activation energies are calculated beforehand by ab-initio calculations and then used in KMC simulations as fixed values. KMC simulation can than be compared with

experimental data, serving as an effective "bridge" between ab-initio calculations and real systems [15].

3 The STM technique

The Scanning Tunneling Microscopy (STM) was first used by Gerd Binnig and Heinrich Rohrer in 1982 (awarded Nobel Prize in 1986). An STM, contrary to other microscopes, does not need any external source of electrons or photons and no type of lenses. The source of information are directly the electrons from the current between the sample and the tip. STM can be used to study conductive or semiconductive samples, but runs into great difficulties when used on insulators. STM provides topographical information in real space and information about the local electronic structure and can be even used to observe in real time processes like diffusion or chemical reactions. The STM tip can be also used for manipulation with individual atoms on the surface, thus manufacturing nanostructures one atom after another. In this chapter, the overview of the STM technique will be presented together with difficulties connected with its realization.

3.1 Principles

The underlying principle of the STM is the quantum tunneling effect. The STM probe, a very sharp metal tip (tip radius 10-100 nm), is approached close to the sample. When voltage V is applied between the tip and the sample, electrons tunnel through a barrier from filled states of the negatively charged electrode to the empty states of the positively charged electrode. The tunneling current I is strongly dependent on distance d between the tip and the sample [16, 17]:

$$I = Vf(V)\exp(-2\kappa d), \quad (18)$$

where

$$\kappa = [(2m_e/\hbar^2)\Phi(V)]^{1/2}, \quad (19)$$

where the function $f(V)$ describes the tunneling barrier, m_e electron mass, \hbar Planck constant and the $\Phi(V)$ is effective height of the tunneling barrier. The κ is of the order of 1 \AA^{-1} , so, for a typical STM current of 1 nA, the tip-sample separation is approximately 1 nm. Note that the meaning of the "tip-sample distance" is not clearly defined and is usually used as an approximate value. On the other hand, it is possible to set an arbitrary plane parallel to the sample surface and compare the tip position to this plane. In praxis this plane is set by choosing some combination of tunneling current and voltage. The position of the tip with respect to the sample under the chosen conditions is called "set point".

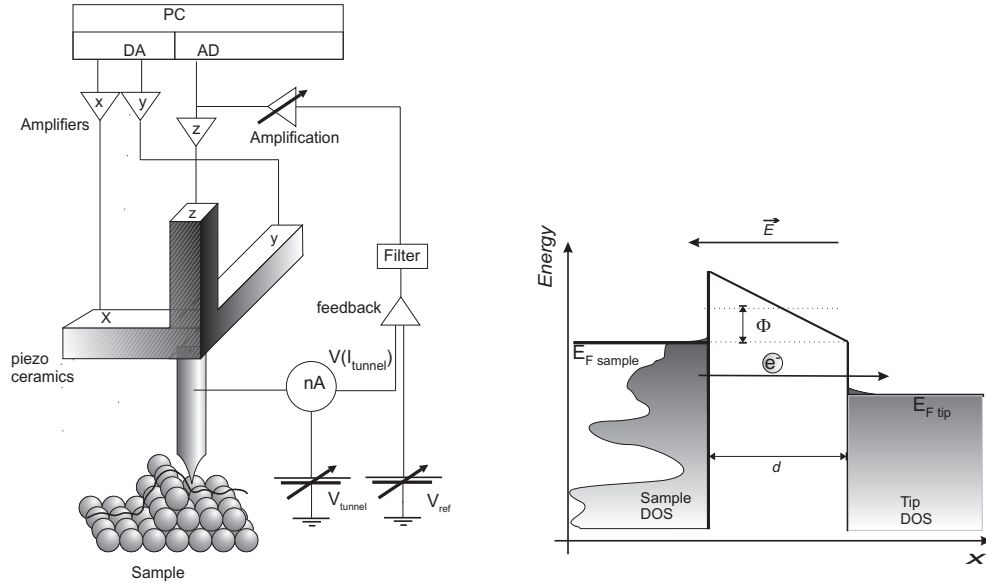


Figure 3: Schema of the setup of the scanning tunneling microscopy (left). Tunneling effect (right) E_F is the Fermi energy level in the tip and the sample, d is the effective tunneling barrier distance, E is the applied electric field, Φ is the effective barrier height.

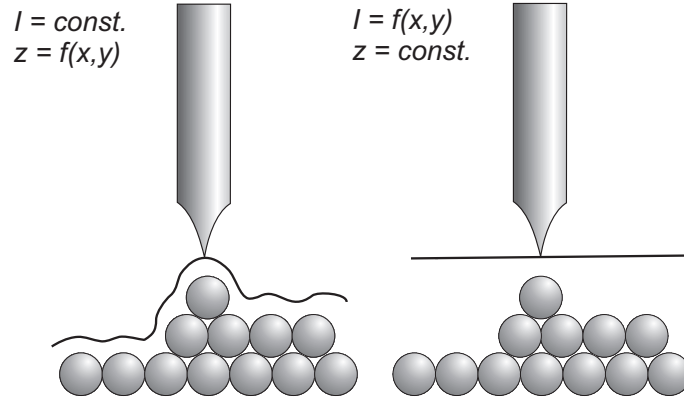


Figure 4: Principle of the constant current (left) and constant height (right) modes.

3.2 Implementation

The position of the tip is controlled by three piezoelements: x , y , z . The x and y directions are used to scan the substrate one line after another. The piezocrystal controlling the z -element is connected into a feedback circuit that allows for keeping a constant value of the tunneling current by adjusting the tip-sample distance. By measuring the voltage applied to the piezoelements we can determine the tip position.

The STM can obtain atomic resolution. Since the tunneling current is exponentially dependent on the tip-sample distance, most electrons flow through the very last atom. The precision of determining the x and y coordinates of the scanning tip is given by accuracy of the voltage applied to the piezoelements and is usually 0.1 \AA . The resolution in direction perpendicular to the surface depends on the accuracy of tunneling current measurement, feedback loop stability and on random fluctuations of the tunneling current. A current measurement error of 2% means approximately 0.1 \AA . The image resolution also depends on the current density distribution in the conductive channel between the tip and the sample and on its dependence on the tip-sample distance.

Two basic scanning modes are commonly used (see Fig 4):

- **the constant height mode** – the z position is fixed, as well as the sample voltage. The information is obtained from the current signal, that is highly dependent on the tip-sample distance. This mode can be used for atomically flat surfaces only, without any high objects in the investigated area, because the tip could crash into such objects.

- **the constant current mode** – An electronic feedback changes the z position during scanning to keep the tunneling current constant. The information is gathered from the z signal. In case of a homogeneous density of electron states the tip follows the surface relief. A disadvantage of the constant height mode is a relatively slow scanning speed given by the finite response time of the feedback loop, but the tip is not likely to crash into sample or move out of contact.

When interpreting the STM images one must remember that the tip does not image atoms, but the distribution of the density of states in the area. It is for example possible, that a single atom is imaged as two "balls" in STM, or that an atomic cluster is imaged as a single ball. For interpretation of an STM image we must consider models of the surface obtained by other methods.

3.3 STS and LDOS maps

With respect to polarity of the applied voltage the electrons tunnel from the tip or from the sample – to the empty or from the filled surface states protruding to the vacuum above the sample. By measuring the $I(V)$ dependency in a fixed tip position, the local density of states ρ can be obtained as [18]:

$$\rho(x, y, z, V) \approx \frac{\frac{dI}{dV}}{\frac{I}{V}}, \quad (20)$$

considering a metal tip. The method based on this approach, scanning tunneling spectroscopy (STS), obtains the local electronic spectrum from the graph of $(dI/dI)(I/V)$ vs. V . Since STM can image in both occupied and unoccupied states, one can also measure spectrum of the unoccupied space, which is an advantage compared to most other electron spectroscopies.

In an STM image, all electron states up to the applied voltage contribute to the total tunneling current. However, the applied voltage range is by principle limited to $\pm\Phi/e$. Using the lock-in amplifier technique, it is possible to obtain an image where only electrons from a certain level contribute [19].

3.4 Variable temperature STM

At room temperature it is only possible to observe processes with rates of similar order as the frequency of acquisition of the STM images (in range from seconds to minutes). To study processes much slower or faster than STM frequency one may

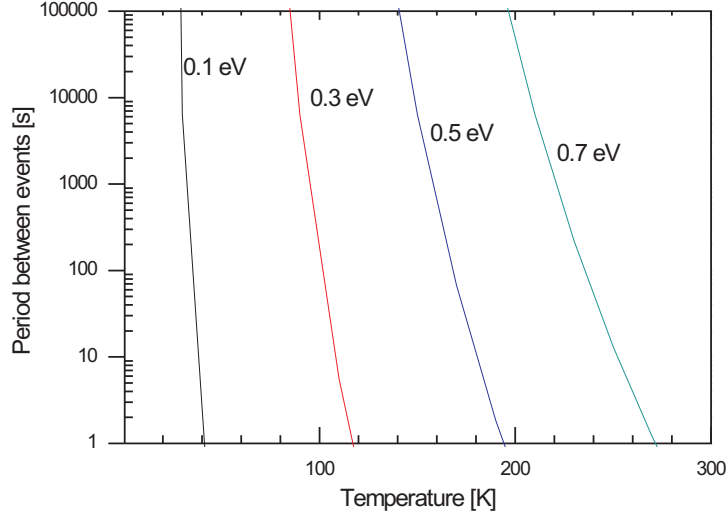


Figure 5: Temperature dependence of mean time between subsequent events shown for different activation energies. The period t is calculated from Eq. 1 as $t = 1/f$ with prefactor $\nu_0 = 10^{13} s^{-1}$. Setting the proper temperature is necessary for real-time STM observation with imaging frequency in order of seconds or minutes.

set the appropriate sample temperature to tune the rate of the processes using Eq. 1 (see Fig. 5).

Heating is usually realized by passing direct current through the sample or the sample holder, or by radiation heating; cooling down is done by thermally connecting the sample with a cryostat at liquid nitrogen or helium temperature [20]. Well defined thermal connection of the sample with the cryostat and precise temperature measurement are necessary.

If the sample temperature is not stable, thermal drift destroys the resolution of STM images (Fig. 6) and makes longer investigation of one area very difficult. This problem can be solved by careful STM design implementing materials with similar thermal expansion coefficients, thermal shielding of major heat sources and symmetrical design of the STM head and by software compensation of the drift: a computer program compares two consequent images using cross-correlation function, computes the rate and direction of the thermal shifts and adds a signal to compensate. (Fig. 6).

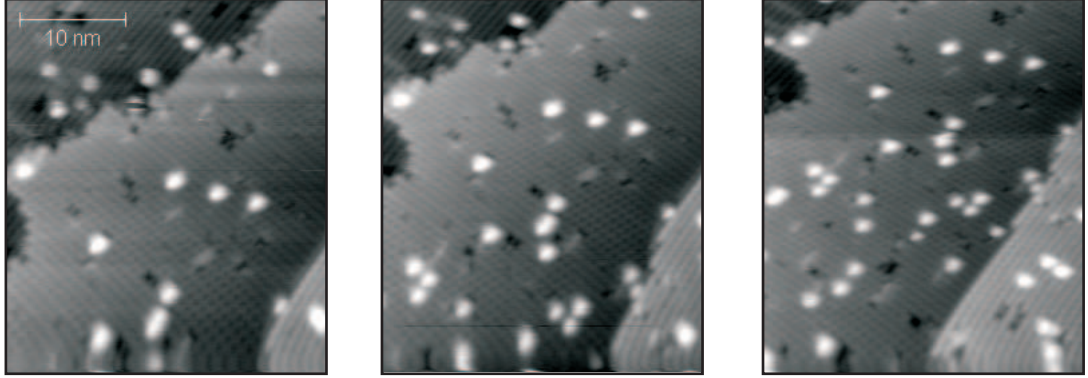


Figure 6: STM image of In/Si(100)-(2 \times 1): Three subsequent images are shifted due to thermal drift of the sample. The distortion of the lower parts of the images is caused by the creep of the piezoceramics - hysteresis of the ceramics when the tip moves from the top area (end of the last image) to the bottom (start of a new image).

3.5 Real-time STM observations

There are two basic types of STM experiments:

1. The static experiment – the studied structure is prepared, transferred to an STM position (chamber) and examined. The advantage of this procedure is low influence of equipment for sample preparation on STM measurement and relative simplicity.
2. The *in – vivo* experiment – the structure is prepared during scanning and its evolution is recorded as a sequence of images. The processes most often studied in this way are diffusion of adsorbed atoms or molecules [21, 22, 23, 24, 25], chemical reactions on surfaces [26, 27, 28, 29, 30] and growth of surface reconstruction [26, 27, 31]. The tip screens the surface from the deposited material. Unless the surface mobility is high enough to transport adatoms into the scanned area, an extraordinarily sharp tip is required to minimize the screening effect. Also, the tip is scanning during deposition - this exposes each part of the scanned area to the flux of adatoms for at least a limited time.

3.6 Diffusion measurements

The tracer diffusion coefficient and magnitude of activation energy of diffusion can be directly measured using STM by tracking a single atom on the surface [32, 33]. The atom can be tracked by means of another feedback loop operating in the x - y plane. In this case, the tip is permanently positioned above the atom and follows its diffusion pathway. The advantage of the fast and detailed record of the pathway is offset by the fact that the tip influences the observed atom (induces strong electric field, injects electrons/ holes). Another measurement of the diffusion coefficient would be subsequent imaging of the area with the migrating atom. The average time lapse between two subsequent jumps must be significantly larger than time lapse between two subsequent images of the scanned area. Cooling of the substrate may be necessary to reduce the hopping rate. Care must be taken not to influence the atom movement by presence of the STM tip (suitable tunneling current, voltage and scanning speed). The second method brings far less influence on the atom, but some jumps may be omitted.

3.7 The STM tip

The STM tip is the crucial part of every STM machine. An ideal STM has the following properties:

- is stable
- is metallic (i.e. has metallic electronic structure, no bands, gaps etc.). This property is necessary to get resolution at all scanning voltages and for acquisition of tunneling spectra.
- is sharp, with the very tip comprising of a single atom, tip radius ≈ 10 nm. Single atom or cluster of atoms at the tip ensure good image resolution, while small tip radius is necessary for deposition of material under the tip.
- does not interact with the sample chemically

STM tips are commonly manufactured from tungsten, platinum, iridium, gold or titanium wires. The sharpness can be achieved by defined cut of the tip, but most often by electrochemical etching. Schematics of the etching used in our group is on Fig. 7 a). A simple electronic circuit (Fig. 7 b)) provides fast stop of etching current — for the tip sharpness it is crucial to stop the etching current and remove the tip from the solution as soon as possible after detachment of the bottom part of the etched wire. The circuit detects the decrease of the etching

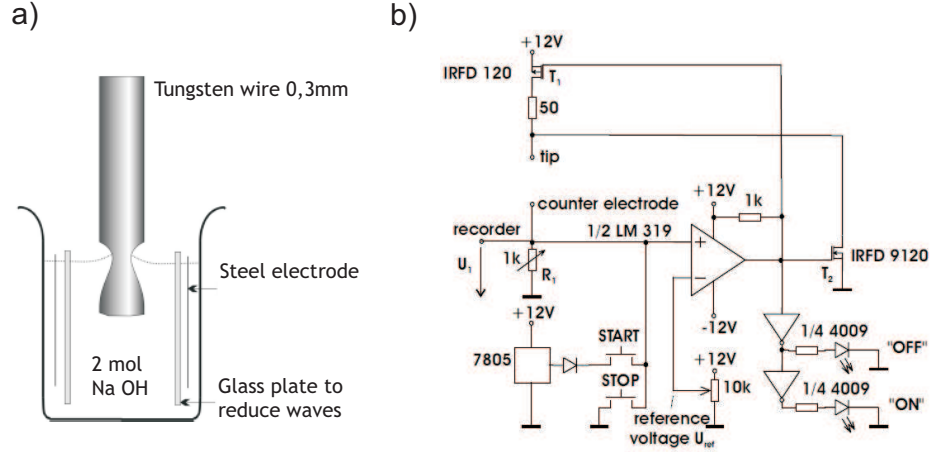


Figure 7: a) - Etching setup for tungsten STM tips. b) The circuit breaks in the moment the wire is etched into two part. The sudden drop of etching voltage is detected and used as signal to stop. Image taken over from [35].

voltage after the wire is etched into two pieces and stops the current. We etch 0.3 mm tungsten wires in 2 mol solution of NaOH. Cylindrical electrode from stainless steel mesh prevents from forming bubbles in the solution and ensures uniform electric field around the tip. Tips are cleaned in hot distilled water and hot ethanol after etching to remove the residual chemicals, then checked in optical microscopes and the best candidates are selected. Tips with tip curvature radius of 20 nm are routinely obtained — see Fig. 8. Once in vacuum, the tips are either heated by electron bombardment (in the KFPP system) or by touching (sideways) a heated W wire (in the FZU AV system) to remove the residual oxide layer and other impurities. As we showed in [34], the electron bombardment can locally melt the tip point, reducing its sharpness. Therefore, we limit the bombarding current to 100 nA. Further cleaning of the tips is done either by repeated heating or by scanning on a Pt crystal. It is also possible to thrust the tip into the Pt crystal in a controlled way or to touch a heated tungsten wire or plate and then "rip-off" a new tip. Any cleaning method involving mechanical contact of the tip end or excessive tip end heating prohibits the *in-vivo* deposition, because though a sharp and metallic cluster may sit on the tip end, the tip as a whole would be blunt and would shield-off any deposited material.

The STM image is a convolution of the functions describing electron densities of the sample and the tip. Therefore, the shape of the tip is also important. If

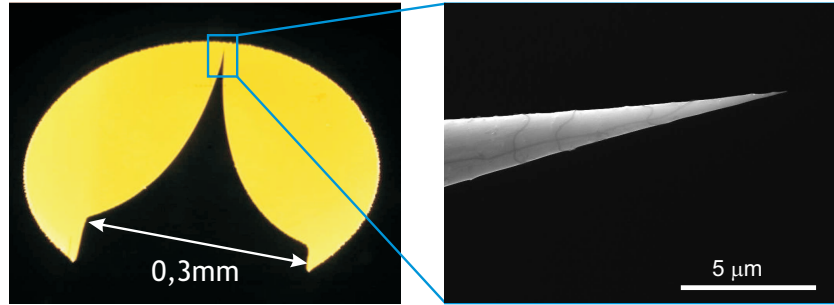


Figure 8: TEM image (left) of the tip and a SEM close-up of a tip end (right).

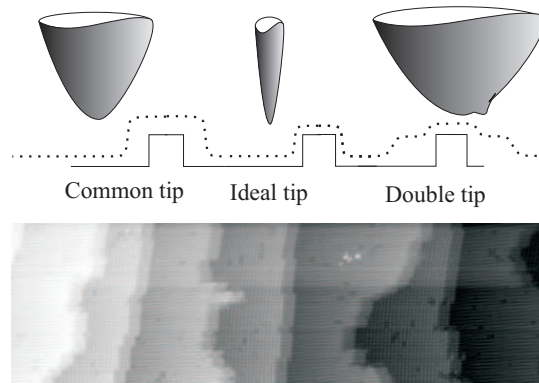


Figure 9: Image of a blunt, sharp and a double tip (above) and an STM image obtained with a double tip (below).

the shape differs from the expected "needle" shape, interpretation of the images and image resolution deteriorates. Most common problem is the "double tip". In this case, tunneling current flows through more than one point on the tip, causing doubling of every image feature (see Fig. 9).

The presence of the tip itself may cause changes to the surface or processes being observed. The tip may introduce contamination to the surface or chemically interact with it or may scratch the surface. The voltage of 1 V applied between the sharp tip and sample with tip-sample separation of ≈ 1 nm causes electric field of order of 10^9 Vm $^{-1}$, The field influences processes both on the surface and on the tip [36] and may cause tip-induced band-bending [37]. The tip allows manipulation with single atoms or molecules: they can be laterally displaced on the surface, lifted up or dropped down with atomic precision [38, 39] and defined

nanostructures can be prepared by high-voltage milisecond pulses or induced field-gradient migration of material from the tip (metal) or from the substrate to the area of the STM contact [40, 41]. The tip interaction can also be unwanted and destructive to the surface. In that case, very low tunneling currents and scanning speed and voltage must be chosen to minimize the negative effects. Controlled interaction of the tip with the sample (current and voltage pulses) is commonly used to treat the tip end.

4 Metals on Si(100)- 2×1

4.1 Introduction

Silicon is the most common metalloid on Earth. It is also the eighth most abundant element in the universe and after oxygen the second most abundant element in the Earth's crust. It was first discovered in 1787 by Antoine Lavoisier. Pure silicon is dark, with reflective bluish surface. For man, the silicon is of extreme importance. It is widely used in semiconductor industry because it remains a semiconductor at higher temperatures than the semiconductor germanium and because its native oxide is easily grown in a furnace and forms a better semiconductor/dielectric interface than any other material. In the last years, the process of electronic device miniaturization has reached such scales that the component size may soon become comparable to interatomic spacings. At these scales, the quantum properties of matter are increasingly important and it is not an easy task to extend the current nanolithography methods to even lower dimensions. Moreover, nanoscale devices can have properties unparallel in the macroscopic world. For this reason, nanotechnology is one of the main research fields today with silicon-based nanodevices being especially intensively studied thanks to its immediate industrial applications and relatively advanced development of the used methods.

Though it is possible to construct devices of individual atoms, this process is time-consuming and impractical for large scale, industrial use. Therefore, so called "self-assembled structures" are being studied. Self-assembled structures are organized structures or patterns that formed spontaneously as a consequence of local interaction among the individual elements of the system. The self-assembly needs certain special conditions to occur, usually the correct combination of materials, temperatures, pressures, electric or magnetic fields and time.

4.2 The Si(100) surface

The Si(100)- 2×1 surface is of high industrial importance. Also, its anisotropic structure serves as a natural template for spontaneous growth of rectangular or 1D nanostructures and so it is an important model surface. The 2×1 reconstruction is well studied [42, 43, 44]. The surface comprises of parallel rows of silicon dimers (a dimer is a pair of atoms). The rows run in the $\langle 1\bar{1}0 \rangle$, while the dimer bonds are orientated in the $\langle 110 \rangle$ direction, i.e. orthogonal to the dimer rows. The dimers are formed to minimize surface free energy: the reconstructed surface has free energy lower by 1.46 eV/dimer with respect to the unreconstructed Si(100). Each dimer saturates two dangling bonds (11). The 2×1 reconstruction exhibits a long-range ordering.

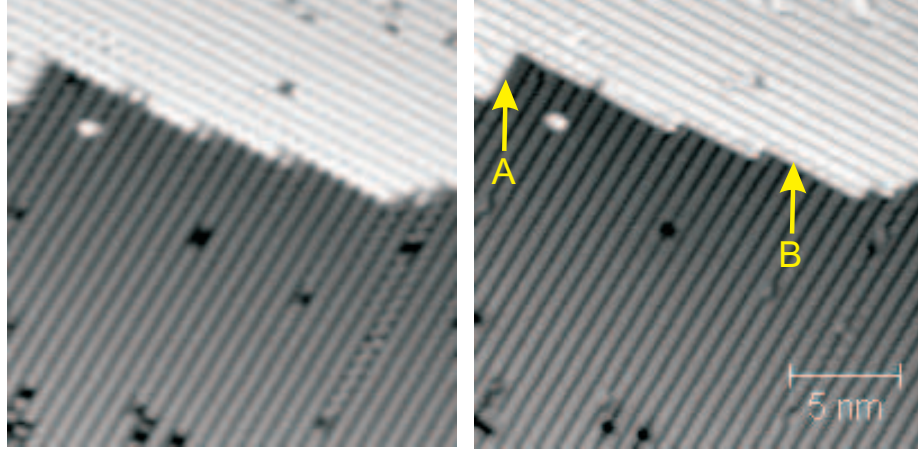


Figure 10: Si (100) surface as prepared. Both types of steps are marked. Left: $U_{tip} = 2.0$ V, $I = 0.1$ nA. Right: $U_{tip} = -2.0$ V, $I = 0.1$ nA.

At the steps on the Si(100)- 2×1 surface the orientation of the dimer rows changes: dimer rows on the upper terrace are orthogonal to the dimer rows on the lower terrace. This creates two types of steps on the surface - when the dimer rows run parallel to the step, the step is called "S-A", when the rows are orthogonal to the step edge, the step is called "S-B" (see Fig. 10).

Low temperature and ab-initio calculations have shown [46] that the 2×1 reconstruction is actually a thermally blurred $p(2 \times 2)$ or $c(4 \times 2)$ structure. In these reconstructions, one atom of the silicon dimer is slightly higher than the other, which is also accompanied by shift of electron density from the lower to the upper atom. This is called dimer buckling. If the buckled dimers in neighbouring dimer rows are "in-phase" the result is the $p(2 \times 2)$ structure, if they are "in opposite phase", the result is the $c(4 \times 2)$ structure. At room temperature (RT) or due to presence of the tip, the dimers in a row are constantly switching between being up and down, so the resulting image is an average of the two states. At temperatures below 200 K or near defects, however, the flip-flop motion is pinned and the $p(2 \times 2)$ or $c(4 \times 2)$ structure is visible - see Fig. 12. Recently published works [47, 48] prove that the ground state of the surface is the $c(4 \times 2)$ structure, but the energy difference to the $p(2 \times 2)$ structure is only about 0.1 meV/dimer and the presence of an STM tip can easily induce transition between the two structures.

The pure silicon has a bulk bandgap of 1.12 eV, the surface bandgap of the the 2×1 structure is ≈ 0.9 eV, the band gap of the $p(2 \times 2)$ and $c(4 \times 2)$ structures

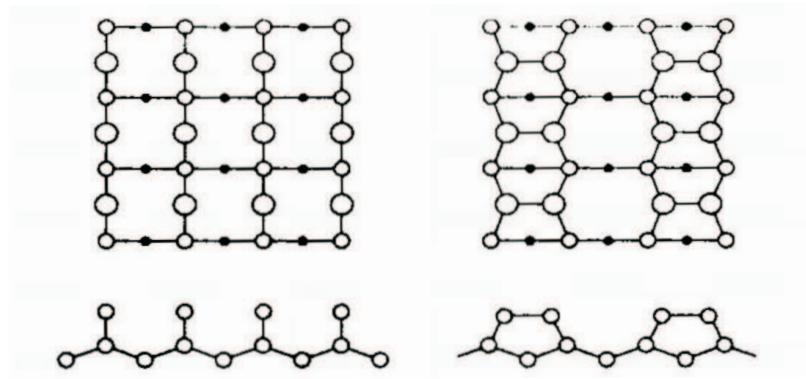


Figure 11: Model of the 2×1 reconstruction. Unreconstructed (*left*) and reconstructed (*right*) surface. Large rings represent adatoms, small rings are 2nd layer atoms and black dots are 3rd layer atoms. Image taken from [45].

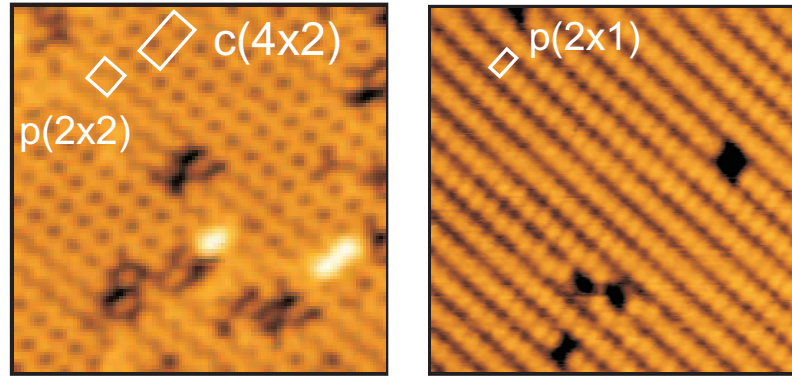


Figure 12: Left: the $p(2 \times 2)$ and $c(4 \times 2)$ structure, filled states, 112K. Right: the $p(2 \times 1)$ structure, result of thermal oscillation of the buckled dimers. Room temperature, filled states.

is ≈ 0.7 eV [49, 50]. Upon formation of a Si-dimer, a σ -bond and a corresponding antibonding state are created. In the symmetric case when both Si atoms are at the same height, the dangling bonds split into two π states (bonding and antibonding). At low temperatures when one atom is shifted up and the other down, two separate states appear (the up- and down-state). At room temperature, the Si-dimers switch between the up and down position, passing through the symmetric position, so the resulting spectrum is a superposition of all the above states.

4.3 Defects on the Si(100)

There are four major types of defects on the Si(100) surface. Three of them were first observed and named by Hamers in 1989 [51]. A single missing dimer in a dimer row is called A-type defect, two neighboring missing dimers form the B-type defect and a dissociated molecule of water is a C-type defect. The fourth is the "split-off dimer" [52], a complicated structure induced by surface stress.

The C-type defect is the most important with respect to growth of metal nanostructures on the Si(100). The C-defect consists of an OH group resting on top of one Si atom and the H atom resting on the neighboring Si atom [53, 54, 45]. In STM filled states, it is commonly resolved as a bright protrusion stretching over two neighboring Si atoms along the dimer row, while the other two atoms of the row appear dark (see fig. 13). In empty states, it only resolves as a darker area instead of two Si atoms. It has been shown that the C-type defect can change its form [45] to two more appearances. The OH and H each saturate one dangling bond, causing the Si atoms look dark in empty states. The brightening in the filled states is caused by a charge transfer from the saturated Si atom to the other Si atom in the dimer.

4.4 Group III and IV metals on Si(100)

The smallest thickness that any wire could have is a single atom wide. If such a wire would be found that is conductive, supported on an insulating substrate and with metallic contacts at both ends, it would be the pinnacle of the classical circuitry. Diverse materials and systems have been studied that more or less approach this ideal. One of such systems are group III and IV metals on the Si(100) surface. Atoms of these metals form chains on the surface that are single atom wide and high (i.e. "1-D or one-dimensional").

These wires can be simply grown by slow deposition of the material on the Si(100) surface at room temperature in ultra-high vacuum.

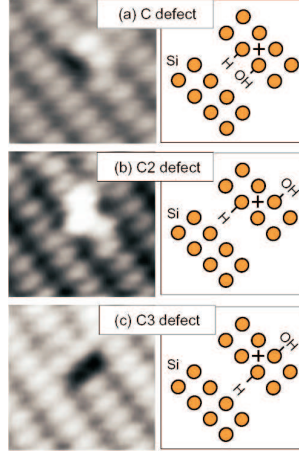


Figure 13: Model of 3 forms of the C-defect and STM image. $U_{sample} = -2$ V, $I_t = 0.6$ nA. The image was taken from [45].

4.5 Group III metals

The first metal of this group studied on the Si(100) was gallium [55]. Ga formed chains of adatoms lying orthogonal to the Si dimer rows. With increasing coverage, the chains became more and more crowded, with island density finally saturating at 0.5 ML (1 ML = 1 monolayer = 6.78×10^{14} atoms/cm²). At this coverage, Ga formed an ordered 2×2 phase. The spacing between the individual Ga chains was $2a$, where $a = 0.384$ nm is the Si unit cell spacing. Similar results were also obtained for Al [56, 57] and In [58, 59]. The metal chains are composed of pairs of metal atoms resting between the Si dimer rows. The metal pairs are parallel to the Si dimers, hence the structure is called "parallel dimer model" [60, 61], see Fig 14. The end of the metal chain can be terminated either by a single atom (monomer termination) or a full pair of atoms (dimer termination). The mechanism that forces the metal atoms to grow as chains was explained by Brocks *et. al* as the *surface polymerization reaction* [62]. In this mechanism, the metal adatom has a strong preference to form a dimer with another adatom (1.1 eV for Al [62]). Each metal atom is bonded to two Si atoms and the other adatom. The bond to the metal adatom changes electronic configuration of the silicon dimers and so the adsorption position "over the row" becomes energetically favourable with respect to other adsorption positions. So, the chain starts growing in the direction orthogonal to Si dimer rows. In the metal chain, each metal atom is bonded to two Si atoms and another metal atom, which means each of the metal valence electron

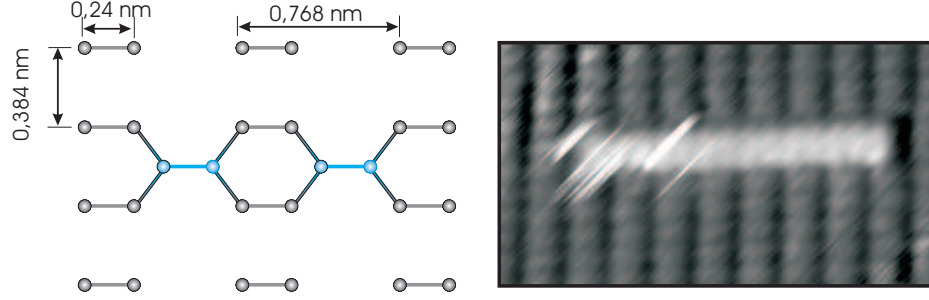


Figure 14: Left - Schematic model of parallel dimer structure. Grey circles represent Si atoms, blue circles In atoms. Right - filled states STM image of an indium chain. On the right side the chain is terminated by a C-type defect, the white stripes on the left side of the chain indicate chain termination with a single In atom. The chain grew in length during scanning, resulting in multiple imaging of the single-atom termination. Scanning direction from right to left.

is covalently bonded. For group III metals, the bonding arrangement is sp^3 like, so there is a completely empty orbital, directed away from the surface. This is clearly visible in STM, where the height of the In chains is 0.3 - 0.5 Å in filled states, but 2.0 - 2.4 Å in empty states. The metal chains exhibit a surface-state band-gap [63], which disqualifies them from serving as wires in nanodevices. At room temperature, only chains containing two or more atoms were observed. For In, a single atom was observed, but only attached to a C-type defect [64]. This suggests high surface mobility of the single atoms.

4.6 Group IV metals

Interestingly, group IV metals on Si (100)-2×1 also grow, in the first layer, as metal chains similar to group III metals. Chains composed of parallel-dimers were observed for Sn [65] and Pb [66]. The growth mechanism and atomic structure of the chains is the same as for group III metals. The extra electron the Sn and Pb atoms have, compared to group III metals, is located in the p_z orbital that is perpendicular to the surface, and may form a π bond. Since this filled state protrudes from the surface, group IV metal chains do not exhibit the height contrast between filled and empty states in STM, like group III metals [63]. STS spectra of group IV metal chains have also shown surface-state band-gap [63].

4.7 Coadsorption of Group III and IV metals

The very similar behavior of Group III and IV metals on the Si (100)-2×1 has led to several coadsorption studies. By simple electron counting we can expect that mixed (group III and IV) dimers would be metallic, as each dimer would carry odd number of electrons. While it is easy to distinguish group III and group IV metal chains in STM thanks to the height contrast [67], it is difficult to properly analyze the mixed islands grown on the surface [68]. Early results suggest, that intermixing with Si substrate or interaction with other chains could affect the grown layer and that special care must be taken when interpreting the STM images. One approach to determine the nature of the mixed structures is the *in-vivo technique* (see Section 3.5). First, a single element is deposited and then, during scanning, the second element is added. So it is possible to identify individual structures based on their known history. For processes too fast to observe directly it is possible to develop a growth model and confirm it with kinetic Monte Carlo simulation. In any case, before one can study the complicate, yet tempting mixed metallic chains, we must first understand the processes that happen when the substrate is covered with only single species adatoms.

5 Experimental Setup

In this section, we provide details about the Scanning Tunneling Microscopes used within the scope of this thesis and about the procedures for sample cleaning, preparation of the 2×1 reconstruction, deposition techniques and temperature control and measurement. The experiments described in this thesis were carried out at the Department of Surface and Plasma Science (KFPP) of the Faculty of Mathematics and Physics at the Charles University in Prague and at the Institute of Physics at the Academy of Sciences of the Czech Republic (FZU AV).

5.1 Ultra-high Vacuum Chamber - KFPP

All sample operations and observations were carried out in ultra-high vacuum (UHV) conditions, as required for observation of clean surfaces (this requirement stems from the demand of impact frequency of residual gas particles so low as to keep the substrate clean for the time necessary for the experiment).

Fig. 15 shows the schematics of the UHV system at the Department of Surface and Plasma Science. The vacuum system is divided to two parts separated with a gate valve. One part contains a triode ion pump continually pumping with speed of 200 l/s. In normal operation, the gate valve is open, allowing the ion pump to evacuate the main chamber. The valve is closed when the main chamber is vented for tip/ sample change or repairs. So, vacuum is not interrupted in the ion pump section. The main chamber with the STM head is pumped with a titanium sublimation pump (TSP). The TSP pump is used every morning. A block valve separates the main chamber from a turbomolecular pump Varian Turbo-V 70 LP with speed of 75 l/s. The primary pump is the Drytel 31 unit combining the membrane and drag pump. The system base pressure is 3×10^{-9} Pa.

The system is baked every time a new sample or tip is inserted. After overnight pumping by the two pumping units the apparatus is baked up at 120°C for approximately 24 hours. The heating is ensured by current-heated spirals inside the chamber and by heating belts wrapped around the system and covered with Al foil. After cooling down, disconnecting the primary pumping units, connecting the main and ion-pumping part again and after evaporating titanium in the main part the pressure decreases to the bottom of the 10^{-9} Pa region.

Vacuum in the system is measured with two ionization vacuum gauges - one in the ion pump part (Varian) with a limit of 3×10^{-9} Pa and the second in the main part with a limit of 10^{-7} Pa (Minionvac KU 803) used during pump-down from atmospheric pressure and baking out.

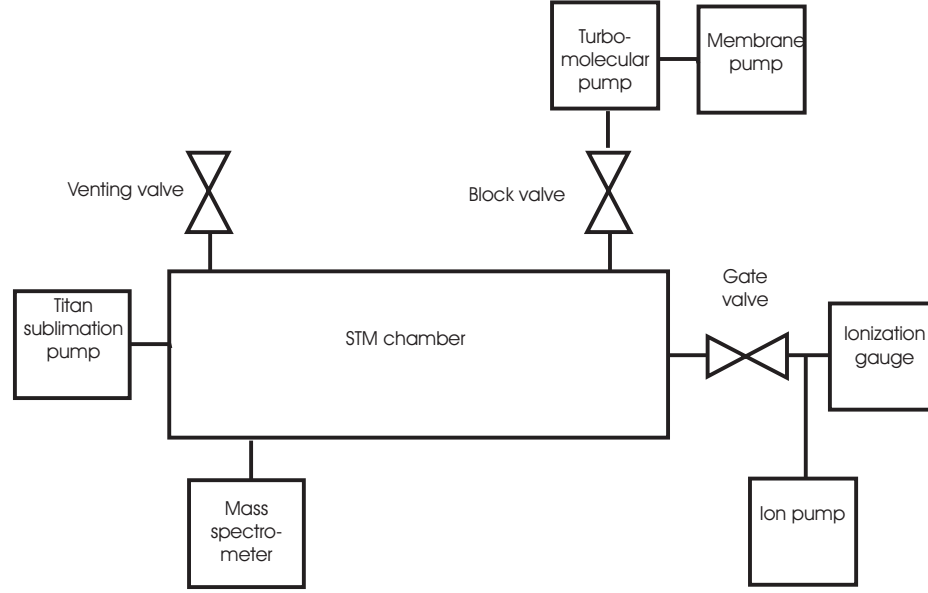


Figure 15: Schematic of ultra-high vacuum setup at the Department of Surface and Plasma Science

5.2 STM head

The schematics of the non-commercial STM head in the KFPP STM system is on Fig. 16. The head is suspended on springs (1) and damped by means of an eddy current damping system to suppress transferring outer vibrations. The linear motor, "inchworm" (2), moves the tip (3) towards the sample. The samples are located on a rotary carousel (5) suspended on a base plate (4), rotated by a set of gears (8). The carousel carries two samples, one Pt crystal, tip-flashing cell and a tungsten sheet plate for tip cleaning. Thickness of the deposited layer is measured by crystal balance (6). A back plate (7) protects the STM head against the deposited flux. The tip, inchworm, lock (10) and *in-vivo* evaporator (13) are mounted on a plate (9). A feedthrough (11) enables transfer of motion and another two feedthroughs (12) serve for electric connections from the non-vacuum part. A photo of the custom-made STM head can be seen in Fig. 17.

5.3 Ultra-high Vacuum Chamber - FZU AV

The FZU AV laboratory is equipped with Omicron SKALA VT-STM system. It's schematics is shown in Fig. 18. The vacuum main chamber is pumped with

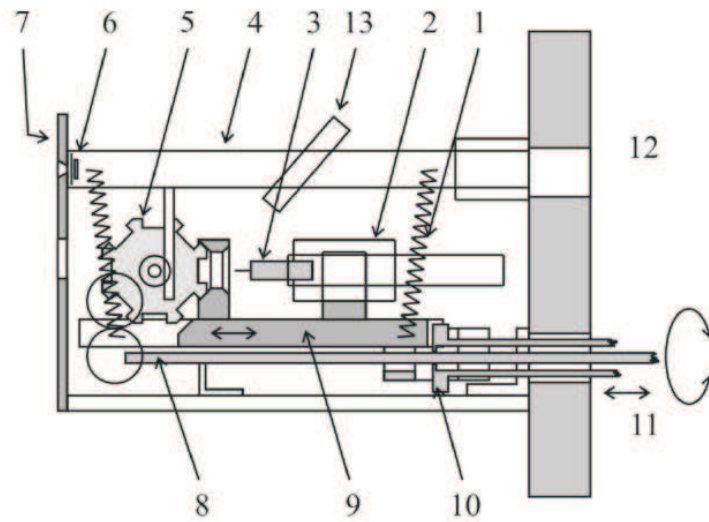


Figure 16: Schematics of the non-commercial STM head. Image taken over from [35].

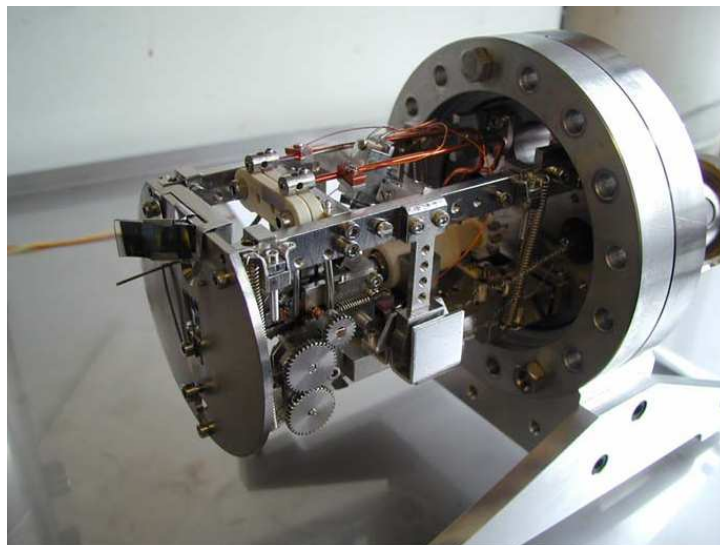


Figure 17: Details of the non-commercial STM head. Image taken over from [35].

ion sputtering pump and TSP pump. Rough pumping is ensured with a combined turbomolecular and membrane pump. The pre-stage is connected to the main chamber through a load-lock, that enables sample replacement in the main chamber without breaking the vacuum. The load-lock and the main chamber are separated with a gate valve. Vacuum in the system is measured with an ionization vacuum gauge. The base pressure in the system is 5×10^{-9} Pa. The TSP is used every morning.

The system has an automatic baking control unit. Baking takes usually 48 hours, while the system stays at the peak temperature of 420 K for ≈ 40 hours. Heating is provided with resistive heaters inside the main chamber.

The chamber is provided with a liquid helium (LHe) cooling system. Helium vapor is pumped out from a LHe Dewar tank with a rotary pump, cooling down a cryostat inside the main STM chamber. Copper wires then connect the cryostat to the sample holder. The temperature is regulated by adjusting the helium flow. The temperature is measured at the cryostat and at the sample holder. Temperature of the sample should be within 5 K from the sample holder temperature up to 100 K and within 20 K below 100 K (Omicron-calibrated). The sample holder can be cooled down to ≈ 30 K, the cool-down time from RT is approximately 45 minutes. Thermal equilibrium between the sample and the sample holder is reached usually within 10 minutes or less. The samples are stored in a separate carousel in the STM chamber and are inserted into the head with a wobble stick.

5.4 Sample treatment

The samples are held on a rotating carousel inside the main chamber. Each time a new Si sample is introduced, it is first degassed at 770 K for 24 hours by direct current heating and then cleaned by repeated flashing to 1470 K for 5-10 seconds. The pressure stays below 1×10^{-8} Pa during degassing and below 1×10^{-7} Pa during flashing. Polarity of the heating current is reversed after several flashes to prevent electromigration effects.

STM measurements at elevated temperatures can be provided by resistive heating of the sample in both KFPP and FZU AV laboratory, scanning below RT only in FZU AV. Temperature of the sample in KFPP is calibrated using a thermocouple glued to the sample after each series of experiments. The sample is then returned to the UHV chamber and heated using the same parameters as in the experiments.

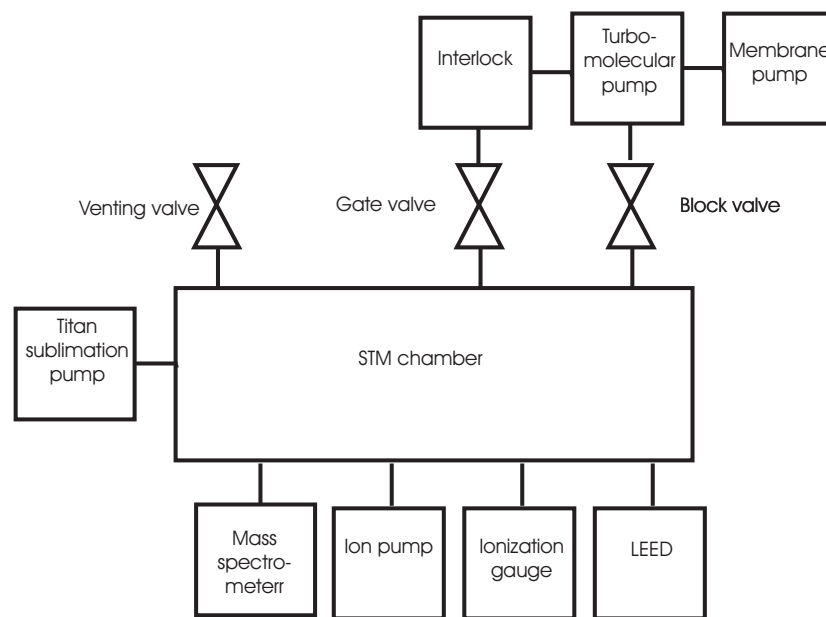


Figure 18: Schematic of ultra-high vacuum setup of Omicron SKALA VT-STM system

5.5 Deposition

In the KFPP system, three evaporators are available: two evaporators capable of simultaneous deposition of two different metals. Their deposition rate is calibrated with a quartz crystal. Deposition rates as small as 0.003 ML/s (monolayer per second) can be achieved. The third evaporator enables *in-vivo* deposition. The deposition rate is calibrated by direct observation of the deposited material in STM. Deposition rates as small as 5×10^{-5} ML/s can be achieved. All three evaporators are tungsten spirals heated by direct current, inside which the required material is placed.

In the AV FZU system, we used an Omicron PN01037EFM electron beam evaporator. Since we discovered that not all charged particles were deflected from the deposition beam by the original design and the extra energy carried by these particles affected the grown layer, we modified the original design by adding a neodymium magnet. After this modification, for low deposition rate (below 0.005 ML/s and low voltages (below 400 V) the current of charged particles to the sample was below measurable limits (0.05 nA). The deposited In purity is 99,99%.

6 In chains on Si(100)-2×1

6.1 In at room temperature

Room temperature experiments with indium on the Si(100)-2 × 1 reconstruction were conducted in the laboratory of Department of Surface and Plasma Science of the Charles University. All experiments were carried out in our non-commercial UHV STM at room temperature with base pressure $< 3 \times 10^{-9}$ Pa. Si(100) samples were cut from an n-type, Sb doped silicon wafer with resistivity ≤ 0.014 Ωcm . To obtain the 2×1 reconstruction, samples were flashed several times for ~ 20 s to $\sim 1200^\circ$ C. We used tungsten electrochemically etched tips. Indium with 99,99% purity was deposited from tungsten wire evaporators either before or during imaging the surface by means of STM. In the latter case, the miniature evaporator was in a distance of 4 cm from the sample and the beam of In atoms was determined by means of two apertures (1 mm diameter). Incidental angle of the deposited flux was 30° . The apex shape of the tip enabled deposition of the In atoms "under" the STM tip, into the scanned area. The thermal drift during deposition was compensated by the STM control unit.

6.2 In chain structure

Before deposition of In, the surface was checked with STM that the sample is clean and that the 2 × 1 reconstruction is present. After deposition, chains of In appeared, see Fig. 19. The chains can be up to tens of nanometers long and are always separated by a distance of at least $2a$ ($a = 0.384$ nm, surface unit cell spacing). The chains never cross terrace steps.

Line profiles of the chains in the filled states show periodically alternating pairs of maxima located between and on top of the Si dimer rows. This is in agreement with theoretical prediction [60, 69] for the parallel dimer model. The primary maximum is located above the In-In bond, the secondary maximum represents the charge redistribution between the up and down Si atoms (see inset of Fig. 19).

In empty states, the empty hybridized $s + p_z$ -orbitals protruding away from the surface overlap. The chains appear much higher in empty states (≈ 2.2 Å) than in filled states (≈ 0.5 Å). Their geometric height is about (≈ 1.3 Å).

The length of chains often changes between subsequent images, but very often one chain end remains fixed. The variation of chain length shows that atoms detach from the chains, migrate on the surface and then attach to other chains. Fig. 19 shows the observed types of chain ends. Using the *in-vivo* technique, the origin of the three different chain ends was identified. We call the termination

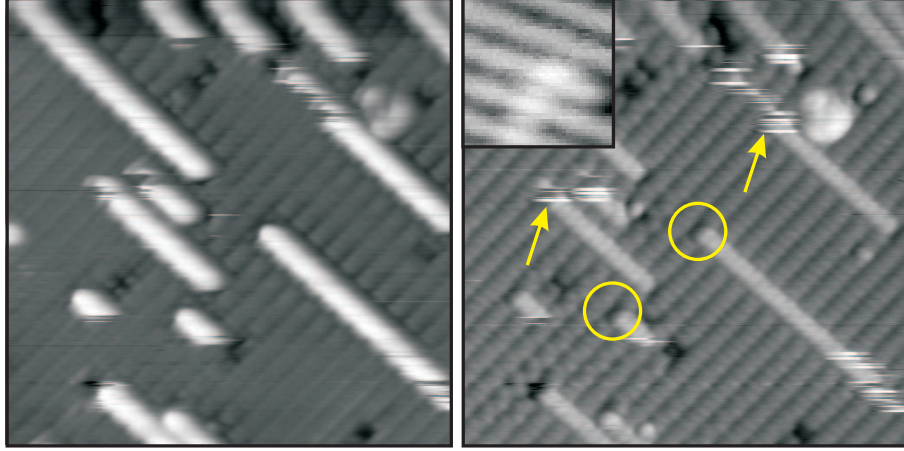


Figure 19: Example of In chains on the Si(100). Empty (left) and filled (right) states image. Area size 20 nm, tunneling current 0.3 nA. Circles mark chain terminations by a C-defect, arrows mark where termination changed between monomer and dimer during scanning. A detail of the dimer termination is shown in the inset.

when the apparent height of the terminating atom is the same as in the middle of a chain as "normal termination", when it is much higher as "bright termination" and the termination with a dark depression as "CD-termination". *In-vivo* growth observation showed that the CD-termination appears when a chain starts growing on a C-type defect - see Fig. 20. The termination of the growing chain then switches between the bright termination and normal termination. Bright and normal terminations were also observed for Ga [70], but never for Al. Observations of a chain decay shows that a C-type defect remains at the place of the CD termination. Once a chain starts growing from a C-type defect, In atoms never nucleate on the opposite side of the defect. Also, the chain never decays from its CD termination. Splitting In chains in two or detachment of atoms from the middle of the In chains was never observed, not even when destroying the chains by voltage/current pulses.

Based on the line profiles and the chain model presented in Fig. 21 we proposed that the "bright" protrusion in filled states at the chain end indicates chain termination with a single atom (monomer), while the "normal" termination indicates a termination by pair of In atoms (dimer termination). A dark protrusion at the CD-termination is explained as termination with a C-defect. The dark area indicates the position of the OH and H groups. Since OH and H saturate the Si dan-

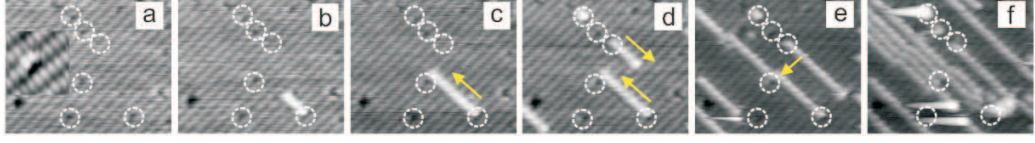


Figure 20: Sequence of images taken during deposition (tip voltage +2 V, tunneling current 0.3 nA). The C-type defects are marked by circles. (a) surface before deposition, the inset shows a form of the C-defect. Arrows in (c) and (d) indicate the growth direction of the chains. (e) a chain "kink" near the C-defect. The bright "flags" in (f) indicate chain ends terminated by a single atom (monomers). The images were taken after 24 min (b), 27 min (c), 30 min (d), 36 min (e) and 53 min (f) from starting deposition. Image size: 13×16 nm². Image taken from [71].

gling bonds, no chain can grow on that side of the C-defect. The charge transfer induced by the C-defect makes the adsorption position on the side opposite to the OH and H group energetically more favourable, similarly to the surface polymerization reaction, so a chain is more likely to start growing there. Compared to the dimer termination, C-defect termination is very stable at room temperatures, so eventually most chains will grow on the C-defects, until all of them are occupied. Only then will chains form that are not terminated with a C-defect.

6.3 In chain evolution

Our experiments, as well as other group's [72] have shown that lengths of In chains can change during scanning. Changes by more than one atom have been observed and voltage pulses were reported to be destructive to the chains [72]. On the contrary, for other group III and IV metals, the chain length was reported stable at room temperature [9, 65, 70]. The parameters controlling the growth/ decay of the In chains were not known. Qualitative effects of the STM tip on the In layer were not explained. Yet this information is crucial to further study the growth mechanisms and stability of the indium chains.

Detachment of the end-atom from a chain is a thermally activated process (see Eq. 1 in Sec. 1) and therefore can be characterized with an activation energy and frequency prefactor. In the first approximation, we might consider it as the In-In dimer bonding energy plus the diffusion energy of a single adatom. Based on the ab-initio calculations, for Al [62] this would mean ≈ 1.2 eV and for In [72] ≈ 0.9 eV. As we will show, we were able to measure the activation energy E_{detach} for atom detachment from a chain and the frequency prefactor ν_0 using the so called

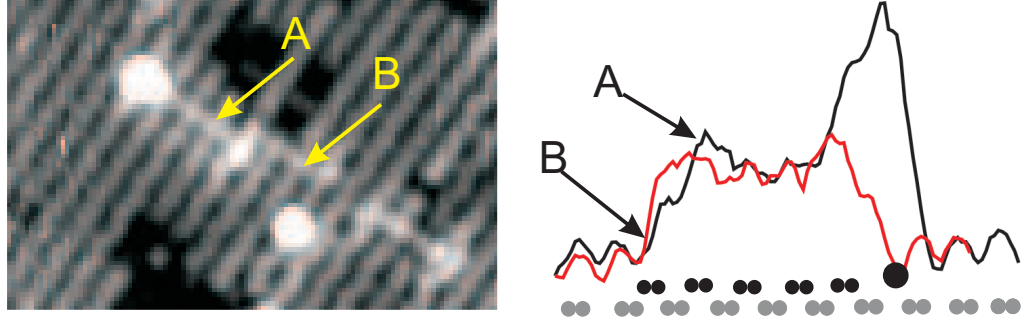


Figure 21: Models of an In chain terminated with a monomer and dimer and the corresponding line profiles. Grey dots are Si atoms, black dots In adatoms. Adding another atom (large black dot) to the chain end changes dimer (B) to monomer (A) termination. $U_{tip}=1.8$ V, $I = 0.1$ nA

”linescanning technique”. The E_{detach} and ν_0 were determined from statistical processing of observed atom detachments from chains at different temperatures, tunneling currents and voltages.

Linescanning technique

Normally, the STM tip scans a square area. In the linescanning technique (see Fig. 22), we only scan a single line (for example above the In chain). The advantage is that we can see changes in the scanned line 512-times faster (since the standard STM image has 512 lines). So, just 0.1 s elapses between subsequent scans of the same point. The disadvantage is the requirement of high tip stability, precise drift compensation and the inability to observe the neighbourhood of the scanned line. The last issue can be solved by imaging the area before and after linescanning or by interrupted linescanning.

Probability of atom detachment

For the experiment we selected only chains not adjacent to other chains or step edges and with free ends (not adjacent to defects, other chains or step edges). We consider the following:

- Free In adatoms on the surface are in thermal equilibrium: the flux of detached atoms is just compensated with capture of adatoms at other nucleation centres.
- Free adatoms follow the Maxwell-Boltzmann energy distribution.
- Atoms only detach individually, not in groups of 2 or more, and only from

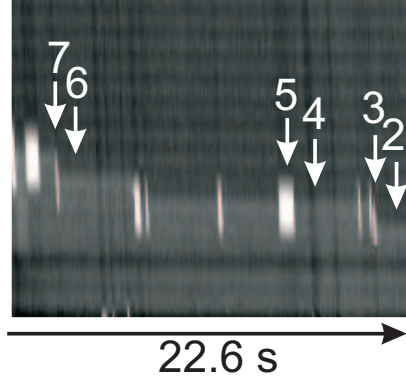


Figure 22: A typical linescanning output showing evolution of a chain. Numbers indicate length of the chain. The chain is terminated by a C-defect on the lower end.

chain ends.

- Chain evolution is a stationary random process. Detachment from the chain is a Poisson process.

We neglect the effects of the surroundings on the chain evolution, though we selected only isolated In chains for the statistics.

The system (In chain) can switch between two states, dimer-terminated (state *A*) and monomer-terminated (state *B*), with 4 processes:

1. detachment of an atom from a dimer-terminated chain.
2. detachment of an atom from a monomer-terminated chain.
3. attachment of an atom to a dimer-terminated chain.
4. attachment of an atom to a monomer-terminated chain.

The processes 1-4 have rates r_1 to r_4 :

$$r_1 = \frac{N_1}{\sum t_A} \quad r_2 = \frac{N_2}{\sum t_B} \quad r_3 = \frac{N_3}{\sum t_A} \quad r_4 = \frac{N_4}{\sum t_B}, \quad (21)$$

where N_i is the count of type-*i* events and $\sum t$ is the total time the chain spent in the condition when the type-*i* event was possible. Let us define a single measurement as starting in the moment when the chain transits from one state to

another and ending when the chain transits to yet another state (lifetimes of states 1 to 4). The lifetimes are random numbers whose distribution (for the detachment processes 1 and 2) is Poisson-type. The probability that within an interval $(0, t)$ no atom will attach or detach from a chain in type A state (dimer-terminated chain) is:

$$P(t) = e^{\frac{-t}{\tau_A}} \quad (22)$$

where τ_A is the mean lifetime of the A-state. The rate r_1 can then be expressed:

$$r_1 = \frac{N_1}{(N_1 + N_3)\tau_A} \quad (23)$$

So, the rate of type-1 event (detachment from dimer-terminated chain) can be obtained as the ratio of count type-1 events to the total time spent in the state A (dimer-terminated chain). Using the formula eq.1 in Sec. 1) we can then express the activation energy E_{detach} to type-1 event:

$$E_{act} = -k_B T \ln \frac{r_1}{\nu_0} \quad (24)$$

Similarly we can obtain activation energy for detachment from monomer-terminated chain.

When the prefactor ν_0 is not known, detachment rates are measured at several temperatures and the prefactor and activation energy can be obtained from the Arrhenius plot. We reformulate equation 24:

$$\ln(r_1) = \ln(\nu_0) - \frac{E_{act}}{k_B} \frac{1}{T} \quad (25)$$

When plotted $\ln(r_1)$ vs $1/T$, the value of the "y-intercept", will correspond to $\ln(\nu_0)$, and the gradient of the line will be equal to $-E_{act}/k_B$.

Data processing and error estimation

A typical linescanning output and a line-profile is shown in Fig. 23. Our custom made program analyses the lines one-by-one and by searching for local maximum/minimum determines the chain end. The user can enter a different chain-end position. The acquired timeline is then automatically fitted with a step function (Fig. 24), dimer-terminated and monomer-terminated life times and atom attachments/detachments are noted. Using Eq. 24 or 25, activation energies for detachment from monomer-/ dimer-terminated chains are calculated.

To verify our results and estimate the measurement and processing error, we programmed a Monte Carlo simulation of the chain evolution using the random

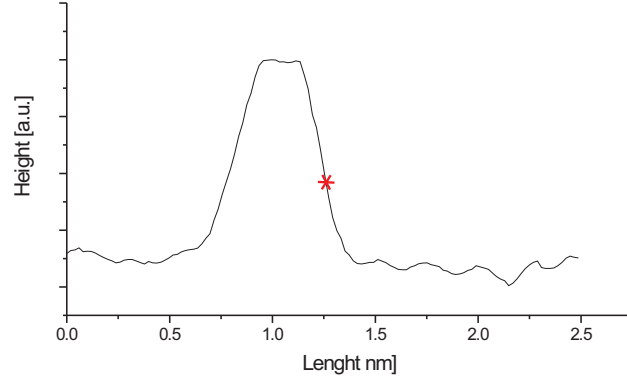


Figure 23: Typical linescanning output and the corresponding line-profile. The asterisk marks the position of the chain end as determined by our program.

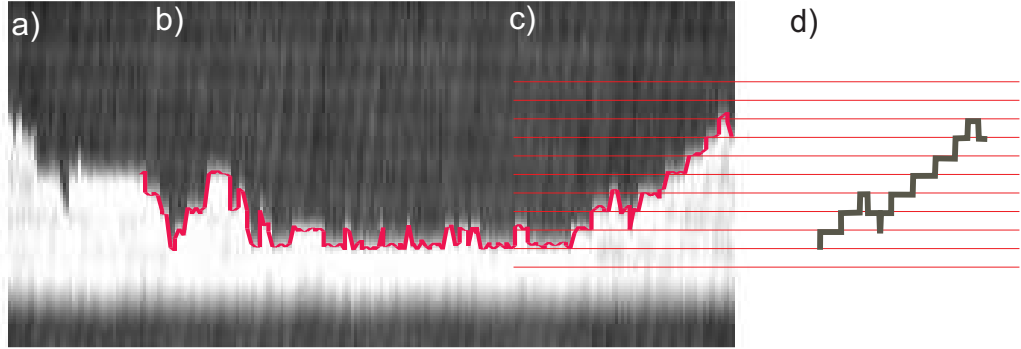


Figure 24: The graphic representation of the chain evolution (a) is transformed into a time series (b). The program smoothes out fluctuations (c) and measures life times in individual states (d) and notes if an atom detached or attached. $U_{tip} = -2$ V.

number generator taken over from "Random Number Generators, Park and Miller, *Communications of the ACM*, Vol. 31, Nr. 10, page 1192" with Bays-Durham mixing. For easy graphical representation of the data we programmed in IDL 6.1. The simulation is kinetic, we are only interested in statistical parameters of the chain evolution. We used the model described in Sec. 6.3.

We introduce three random Poisson processes in the model with the corresponding rates:

- detachment of an atom from a dimer-terminated chain: r_1
- detachment of an atom from a monomer-terminated chain: r_2
- attachment of an atom: $r_3 = r_4$

In pre-set time steps Δt , the program evaluates, if one of the above events occurred (and which one) and if so, changes the chain length accordingly. We do not consider occurrence of more than one event in a single time step. We checked, that the probability of two events happening within a single time step $\Delta t = 0.01$ s is less than 0.0001. Simulation ends after a predetermined number of time steps.

The probability of the three events within one time step of the simulation Δt is obtained by substituting the corresponding rate r_i into:

$$prob_{ri} = 1 - \exp(-r_i \Delta t). \quad (26)$$

Probability of attachment to dimer- and monomer-terminated chain is presumed the same ($r_3 = r_4$). After each simulation run, the program calculates the rates r_i per the formula 23. It is obvious that for large number of events ($N \rightarrow \infty$), this value must match the value input as a parameter. The accuracy of the calculated rates is related to the size of the statistical sample. We ran the simulation with parameters obtained from the experiment and observed the ratio $r_{calculated}/r_{input}$ as a function of number of observed events of the corresponding type N_i . With increasing number of events the ratio converges to 1 as expected. From 100 simulation runs for each combination of parameters we calculated the standard deviations as a function of sample size for various detachment rates r_i (see fig. 25).

The best time resolution of the chain evolution is 10 Hz (events per second). The measured rates are within (0.013; 1.86) Hz, only high temperature detachment rates from monomer end are found to be 8.8 Hz (37.5 °C) and 11.7 Hz (50.1 °C). It is possible that insufficient sampling frequency might affect processing the measured data or completely skip some events (we have observed detachment of two atoms in one time step). To estimate error caused by low sampling frequency we simulated evolution of a chain ($r_1=0.1$ Hz, $r_2=2.0$ Hz) with simulation time

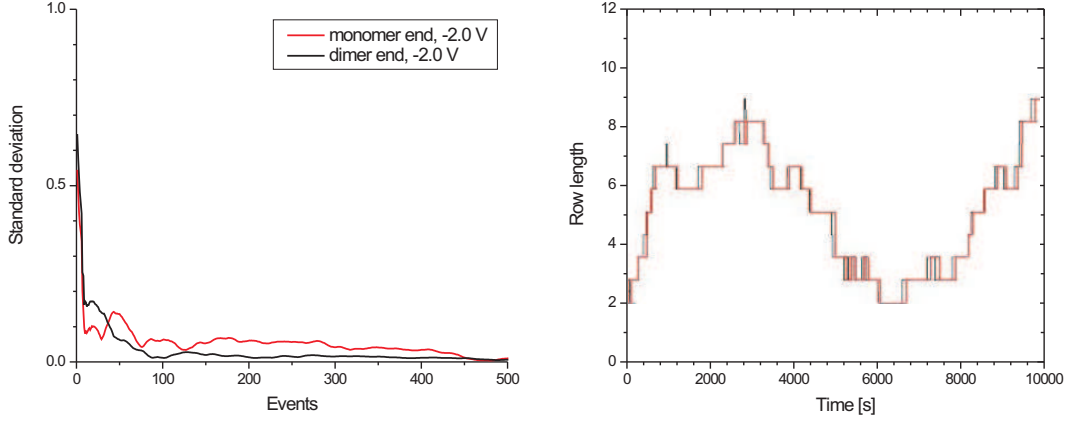


Figure 25: Left: Standard deviation of the detachment rate as a function of observed events shown for the fastest observed rate (parameters for sample bias 2.0 V). Right: Example of an extremely small sampling rate of 1 s. Simulation step is 0.01 s, detachments rates: $r_1 = 0.0135$; $r_2 = 0.708$, $r_3 = r_4 = 0.1$.

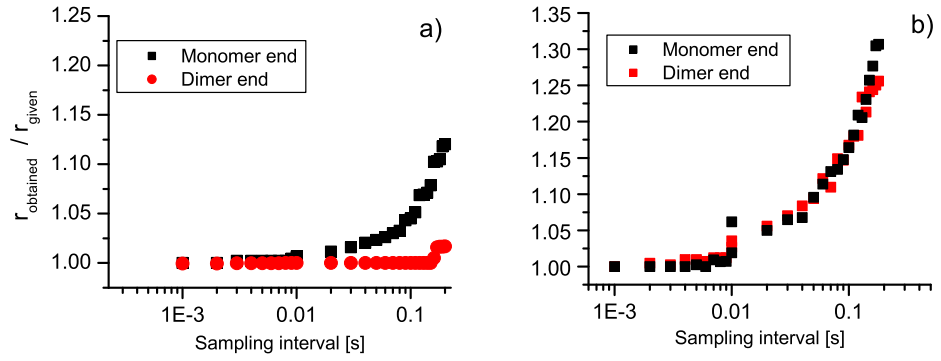


Figure 26: Deviation of obtained rates r_i from pre-set rates as a function of sampling rate. Shown curves correspond to -1.6V (a) and -2.0 V (b) tip bias. It is clear that for our sampling rate (0.10 s/line), the measurement error is less than 15 % for the worst scenario.

step 0.001 sec. Then we analzed this chain using our standard procedure (with sampling frequency 10 Hz). The results are shown in Fig.25.

6.4 Tip influence (Publication 1 - Kocan 2007)

Our first step in the STM study of the indium chains was determining tip influence on the chains. In the first publication, we briefly summarize the linescanning technique and study the effects of scanning speed, tunneling current and tip voltage on the detachment and attachment of In atoms to the chains. The paper concerns only with room-temperature data. The observations can be summarized as follows:

- The chain length can be identified precisely thanks to image contrast in filled states between the monomer and dimer termination.
- C-defects are found to be nucleation centers for the In chains.
- The chain stability depends on the chain length. Dimer-terminated chains are more stable than monomer-terminated chains. A single dimer nucleated on C-defect is found to be the most stable structure.
- Electric field (tip voltage) is observed to have a strong effect on both attachment and detachment of atoms to chains, while atomic forces (scanning speed) and local heating (tunneling current) do not.

Our proposed explanations and results are:

- The higher stability of the dimer-terminated chains is in agreement with parallel-dimer models that found the dimer as the most stable structure for low coverage of In.
- Increased chain stability near the C-defect explains why most chains are grown on the C-defects.
- The higher contrast of the monomer termination ("bright" termination) is caused by half-filled $s + p_z$ orbital of the last atom. It is imaged in both polarities and the stand-up shape of the orbital cause high STM contrast with respect to other (dimerized) atoms of the chain.
- Influence of the tip on In chains on Si(100) can be explained by positive charging of In adsorbate or formation of a static dipole. Then, positive tip bias would repel migrating atoms, reducing the attachment rate, while negative tip bias "traps" the atoms close to the tip.
- Scanning in filled states is optimal due to lowest influence on the chain stability.

The extreme stability of the C-defect termination and the proposed growth mechanism was recently confirmed by an ab-initio study [73]. In this study, based on the density functional theory using local orbital basis, total energy calculations were presented for various scenario of In nucleation on C-defects. The presence of the defect induces a surface state just below the Fermi level, resulting in a surface-mediated reaction forming a chain of indium atoms. Bonding of In at the C-defect is by 0.5 eV more favourable than the equivalent position on the clean silicon surface. Adsorption of a second In atom is even more energetically favourable. The simulated line profiles above a chain of two and three atoms also confirmed that the monomer termination appeared as "bright" termination compared to dimer termination in filled states. In a theoretical study by Albao *et. al* [74], these observations were confirmed and extended to Ga and Al.

6.5 Detachment energies

Fig. 27a shows the Arrhenius plot of the detachment barrier from a monomer- and dimer-terminated chain. Since the detachment rates were found to be dependent on chain length, we present only data with large enough statistical samples (more than 100 events per point): C-defect plus three atoms and C-defect plus more than one In dimers. Data were acquired in filled states to minimize the tip influence. Attempt frequency and detachment barriers can be obtained from the graph:

| | E_{det} [eV] | prefactor ν_0 [Hz] |
|-------|-----------------|----------------------------|
| CD+3 | 0.82 ± 0.01 | $8.7 \times 10^{13 \pm 2}$ |
| CD+2n | 0.87 ± 0.02 | $6.5 \times 10^{13 \pm 1}$ |

Fig. 27b shows the detachment barriers calculated per Eq. 24 using an exponential prefactor $\nu_0 = 6.5 \times 10^{13}$ Hz. From Publication 1 we can also estimate detachment barriers for CD+1 and CD+2 as 0.74 eV resp. 0.93 eV. As expected, the monomer termination is less stable than dimer termination. The effect is more apparent in empty states, when detachment is enhanced by presence of the tip. The obtained detachment barrier agree well with the effective In-In bond energy -0.8 eV, derived by Dong in [72]. In an ab-initio study by Albao [74], the adsorption energy E_{ads}^n of n -th metal adatom to a chain of length $n-1$ on the clean Si(100)-c(4×2) surface were calculated, as well as diffusion barriers E_{diff} for In adatom. If we consider a simple detachment model, where the detachment barrier of the n -th metal adatom E_{act}^n is a sum of the diffusion barrier and the bond represented by E_{ads}^n :

$$E_{det}^n = -E_{ads}^n + E_{diff} \quad (27)$$

using the values from [74] we get:

| chain length | E_{act}^n (eV) | [74] | E_{diff} [74] (eV) | E_{det}^n derived from [74] (eV) | E_{det}^n measured (eV) |
|--------------|---------------------|------|-------------------------|---------------------------------------|------------------------------|
| CD+1 | -0.340 | | 0.272 | 0.612 | 0.74 |
| CD+2 | -0.807 | | 0.272 | 1.079 | 0.93 |
| CD+3 | -0.423 | | 0.272 | 0.695 | 0.82 |
| CD+2n | -0.601 | | 0.272 | 0.873 | 0.87 |

The general trend of dimer-terminations being more stable than monomer-termination is the same in our work and Albao's study, though the detachment barrier differ especially for the CD+1 and CD+2 chains. One possible reason

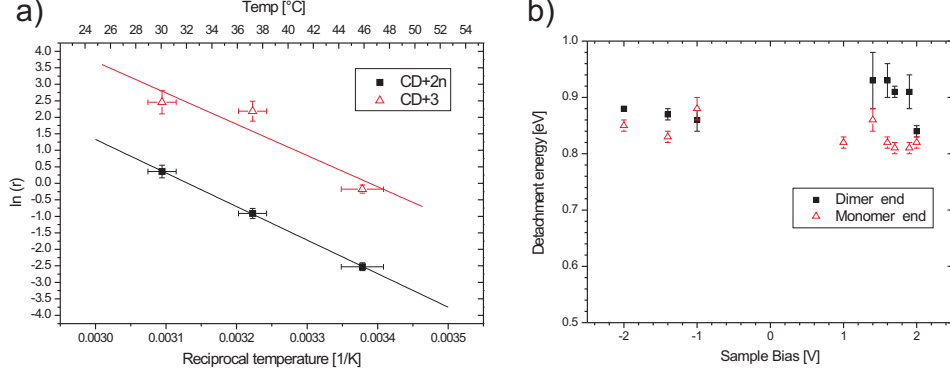


Figure 27: a) Arrhenius plot of detachment rates for chains consisting of a C-defect plus 3 atoms respectively plus more than one In dimer. b) Measured detachment energies as a function of sample bias. $I_t=0.3$ nA, $T = 24.5$ $^{\circ}\text{C}$, sample rate 0,1 s/line. Black squares mark detachment from dimer-terminated chains, red triangles from monomer-terminated.

could be our insufficiently large experimental data set. Another reason might be the relatively small diffusion barriers calculated by Albao. Our preliminary results from study of diffusion of In on Si(100)-c(4 \times 2) at low temperature indicate that the diffusion barriers are ≈ 0.3 eV. To our knowledge, detachment barriers for group III or IV metals on Si(100) have not been measured before.

The attempt frequency ν_0 is commonly used in Monte Carlo simulations of diffusion. For Si(100) an approximate value of $\nu_0 = 10^{13}$ is mostly used [9, 75]. There are no available calculations of atomic vibrations of group III metals on Si(100), but as a rough measure we can use values calculated for Sn [76]. Eighteen phonon modes were discovered for Sn dimers, with the highest peak around 24 meV, which corresponds to $\approx 6 \times 10^{12}$ Hz. Surface phonon energies measured by electron loss spectroscopy [77] and inelastic neutron scattering [78] for clean Si(100)-2 \times 1 yield a value of 1.7×10^{12} Hz resp 1.5×10^{12} Hz. Because In is slightly lighter than Si, we can expect phonon frequencies higher than for Sn, but it is not very likely that they are higher than on clean surface. Our results are rather high, though still within experimental error from these reference values. The measured higher attempt frequency can be attributed to the tip-effect: rather than direct measurement of surface phonon frequencies, we measure an "effective attempt frequency". We point out that these are first experimental results for the attempt

frequency, justifying the value commonly used in MC simulations. For example, on the Si(111)- 7×7 the phonon frequencies are also in the 10^{13} range, but the measured attempt frequency for inter-cell hopping is $\approx 10^{10}$ [32].

6.6 Kinetics of In growth (Publication 2 - Ostadal 2008)

Kinetics of group III metals on Si(100)- 2×1 was so far studied only in a single paper by Albao [9], which considered only gallium. Since the surface mobility of In adatoms is too high at RT to observe diffusion directly, we measured a set of statistical characteristics of In chains. The growth was studied *in-vivo* and real-time measurements were taken of the layer after it reached dynamical balance state. The results are presented in the Publication 2.

We can summarize the observations and findings:

- C-defects are preferential nucleation sites for In chains.
- Average chain length and concentration of chains were measured as a function of coverage and with different concentration of C-defects. Concentration of C-defect controls the average chain length and concentration of chains.
- Chain length distribution (CLD) was measured *in-vivo* and after relaxation. CLD has an exponentially decreasing character in both cases. Little difference between CLD measured during and after growth indicates high adatom mobility, since dynamical equilibrium is reached almost immediately.
- Number of In atoms changed in an area enclosed by In chains. This shows, that "forbidden zones" around In chains do not completely restrict In adatom movement. (Forbidden zone was a feature used in KMC simulations to mimic the observed fact that no atoms or chains were spotted on the sides of group III metal chains.)

Based on these data, we will later present a growth model for In on Si(100)- 2×1 .

6.7 Diffusion of In (Publication 3 - Javorsky 2009)

With respect to findings presented in Publications 1 and 2, we may formulate a physical atomistic model of In chain growth. The Si(100)-2×1 is represented by a rectangular matrix of adsorption positions. The chains grow and decay by attachment and detachment of single atoms at the ends of the chains only. A chain may grow only in the direction perpendicular to Si-dimer rows. A chain is created when an In adatom bonds to another adatom or to a C-defect in the direction perpendicular to Si-dimer rows. An atom will always bond to another atom, C-defect or chain if in a suitable position. An atom directly bonded to the C-defect would never detach in the model. Free adatoms may not enter into the adsorption positions on the sides of a chain (there exist "forbidden zones"), so there is always a spacing of at least one adsorption position between the neighbouring chains. Detachment from the chains is thermally activated. In the model, there are no other defects or surface steps. Based on the model, a Kinetic Monte Carlo simulation was programmed. Output of the simulation is discussed and compared with experimental data. We present the details of the model and our results in Publication 3.

We can briefly summarize the results as follows:

- Extensive statistical characteristics describing In chains on Si(100)-2×1 were gathered.
- We developed and programmed a physical model for the submonolayer growth of indium on Si(100).
- Diffusion barriers for In adatom were found almost isotropic:

| | Parallel detachment | | Perpendicular detachment | |
|---------|----------------------|------------------|--------------------------|------------------|
| | E_{\parallel} [eV] | E_{\perp} [eV] | E_{\parallel} [eV] | E_{\perp} [eV] |
| 0.04 ML | 0.64 ± 0.03 | 0.62 ± 0.07 | 0.64 ± 0.03 | 0.67 ± 0.07 |
| 0.08 ML | 0.62 ± 0.03 | 0.61 ± 0.07 | 0.61 ± 0.03 | 0.64 ± 0.07 |
| in vivo | 0.60 ± 0.10 | 0.65 ± 0.05 | 0.65 ± 0.10 | 0.65 ± 0.05 |

- We show that the monotonous form of the chain length distribution function obtained for indium layers with low coverage at RT and used deposition rates can be explained by the process of atom detachment from indium chains during the growth.
- We show that at RT the system evolves fast within ≈ 10 minutes after deposition, than relaxes for ≈ 6 hours to equilibrium with only minor variations.

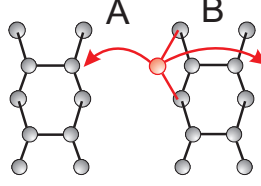


Figure 28: Two possible jumps parallel to In chain (perpendicular to Si dimer rows). A = between dimer rows; B = over dimer rows. In general the jumps have different probabilities, but for simplicity we considered them as equal in our simulations.

- Dependence of average chain length and chain concentration on concentration of C-defects was confirmed by the model.

In a recent *ab-initio* study by Albao et. al [74], the diffusion barriers for group III metals on Si(100) are stated. For In, the barriers are: $E_{\parallel} = 0.272$ eV and $E_{\perp} = 0.269$ eV, i.e. still isotropic, but much lower compared to our results. The reason for this difference might be that our growth model does not consider other types of objects on the surface, like missing dimers and step edges. In reality, these objects block adatom movement or temporarily trap the adatoms, effectively increasing the diffusion barrier. Also, for simplicity we considered the "forbidden zones". Again, the zones hinder adatom diffusion and effectively increase diffusion barrier. So, the barriers calculated in Publication 3 are rather "effective" diffusion barriers. Another reason for the difference between our and Albao's diffusion barriers is that our model does not distinguish between indium jumps "between" two dimer rows and jumps "over" a Si dimer row (see Fig. 28). While these two events should generally have different probabilities, they are considered as equal in our simulation, because the overall migration would be controlled by the less frequent of those two events. (In [74], the calculated diffusion barriers between dimer rows (A) and over a dimer row (B) are: $E_A = 0.18$ eV, $E_B = 0.27$ eV.)

As shown in a paper by Tokar [8], the monotonous form of the chain length distribution is characteristic for a system in the thermal equilibrium. However, in the thermal equilibrium, the shape of the distribution function is no longer dependent on kinetic parameters such as diffusion barriers. So, if the studied system is close to the thermal equilibrium, the accuracy of determining the diffusion barriers based on comparing the simulated and measured statistical properties of the grown layer may be lower than we expected. A possible way to overcome this problem is to measure at lower temperatures, when the detachment of atoms is less frequent and the system is "frozen" far from the thermal equilibrium.

6.8 Low temperature observation of In on Si(100)

The most direct, but experimentally challenging way to observe diffusion of In adatoms on Si(100) is STM observation at low temperatures (LT), when the hopping rate is sufficiently low to observe the diffusion directly. Our low-temperature STM experiments were conducted in the Academy of Science of the Czech Republic at the Institute of Physics.

Indium adatoms on Si(100) are difficult to observe at LT. Below 120 K, it is only possible to scan In/Si(100) in filled states, otherwise the tip crashes immediately. This problem only occurs if In was deposited at substrate temperature below ≈ 120 K. Depositing at higher temperatures and then cooling down allows for scanning in both polarities. We attribute this effect to presence of single In atoms. As we suggested in Publication 1, a charge transfer occurs from the In atoms to the substrate, leaving In positively charged. The negatively biased tip attracts the free In atoms. The effect of the tip field is increased at low temperatures, due to limited screening of the In adatom charge by bulk electrons. Attraction of the free adatoms to the tip may then cause crashing of the tip. This also implies that single In atoms are all captured at chains or defects above 120 K, because at higher temperatures scanning in both polarities is possible.

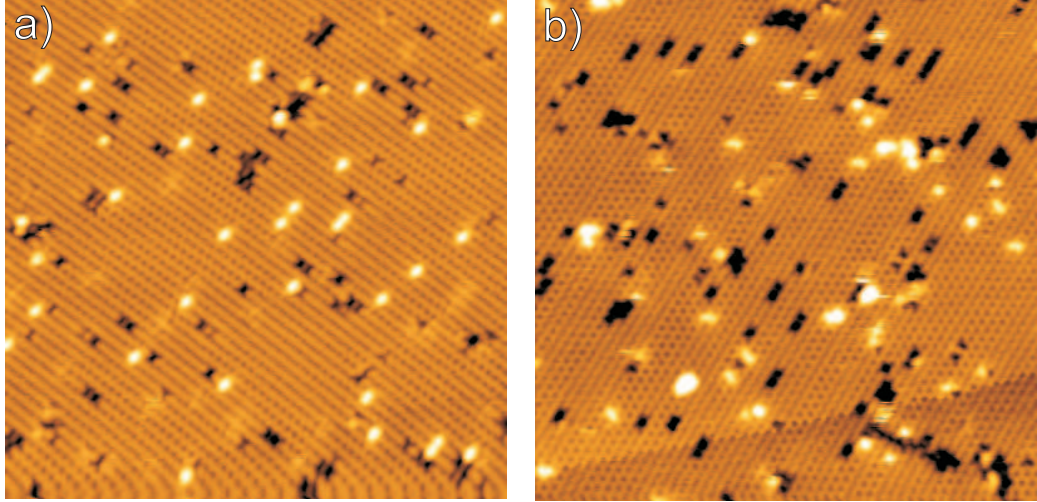


Figure 29: 0.1 ML of In deposited at 30 K, observed at 80 K. In image a) ions from the e-beam evaporator were not extracted, $U_{evap}=700$ V. In image b) the ions were diverted by means of a magnetic field, $U_{evap}=200$ V. The ion current to sample was below 0.1 nA. Scanning paremeters $U_{tip}=1.8$ V, $I = 0.1$ nA.

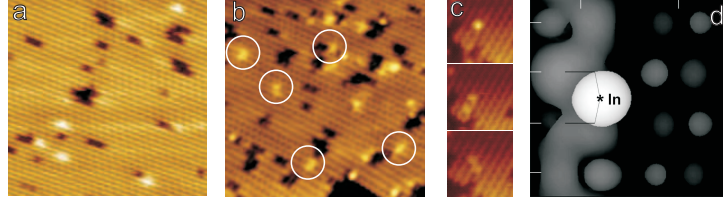


Figure 30: a) In adatom immediately after deposition at 30K. Area 30×30 nm, $I_t = 0.1$ nA, $U = 2$ V. b) The same layer at $T = 82$ K; white circles mark single In adatoms. c) - Sequence showing tip-induced splitting of In dimer into single atoms. d) LDOS plot for a single In adatom bonded to two Si dimers. Taken from [69].

Fig. 29 shows Si(100) with ≈ 0.1 ML In. In was deposited at 30 K in both cases using e-beam evaporator. In the image a) In chains have formed despite the very low temperature. We found that the average chain length is almost similar as for RT. Image b) shows the same amount of In deposited at the same temperature, but an extra 0.1 T neodyme magnet was applied to divert charged particles from the e-beam evaporator. We measured the current of the incoming charged particles falling on the tip. Using the magnet and reducing the electron bombardment voltage to 200 V, the current was reduced below 0.1 nA (the minimum detectable using our electronics). It is apparent that the charged In atoms carried enough energy to migrate on the surface long enough to form chains.

Fig. 30a shows 0.1 ML of In on Si(100) at 82 K. White circles mark the objects never previously observed on the Si(100). These appeared after deposition of In at 30 K. The objects can hop on the surface, join together forming chains or attach to an In chain. They were never observed above 120 K. Fig. 30c shows a voltage pulse-induced split of an In dimer into two of these objects. We conclude that these objects are single In adatoms.

The appearance of an In adatom on Si(100) changes according to surface reconstruction and temperature - see Fig. 30 a-b. While at 30 K the adatoms appear as single bright ovals, at 85 K In appears as bright "dumbbells". Fig. 31 shows sequences of migrating adatoms at 85 K. In adatoms on the $c(4 \times 2)$ reconstruction or where different reconstructions meet appear as bright "dumbbells" orthogonal to Si dimer rows. On $p(2 \times 2)$ the "dumbbells" are rotated by $\approx 45^\circ$. Several ab-initio studies calculated that the In adatom is bonded to two Si dimers belonging to the same row [69, 75, 74]. However, the calculated barrier for hopping between the dimer rows (on $c(4 \times 2)$) is only 0.18 eV [75]. It is likely that at 85 K, the hopping between the Si rows is too fast to observe by STM. STM then shows a

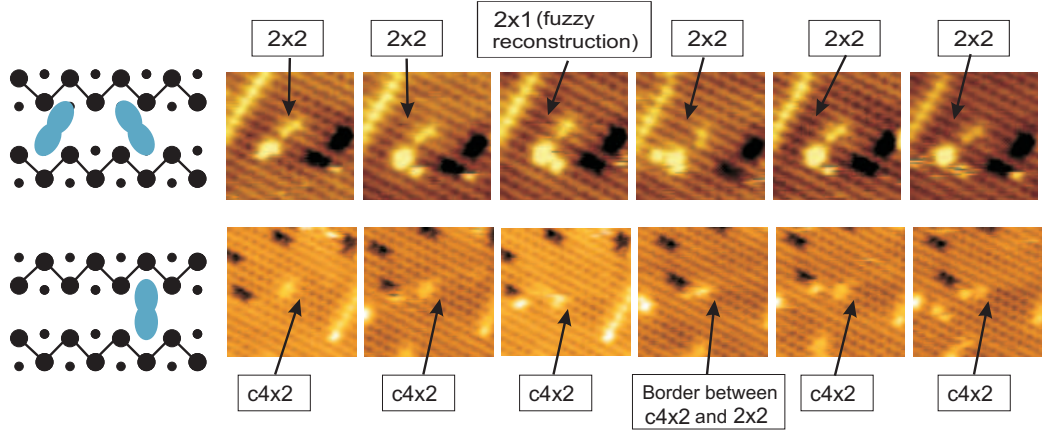


Figure 31: Above: In adatom hopping on $p(2\times 2)$; below: - $c(4\times 2)$. $I_t=0.1$ nA, $U = 2$ V, $T = 85$ K. Model: Large and small black circles represent up and down Si atoms, black line help to match the model to STM image. Blue ovals represent STM images of In adatoms.

time-averaged image of In adatom hopping inside the row. This is similar to an STM image of the flip-flop motion of the Si dimers, which results in imaging the $c(4\times 2)$ reconstruction as 2×1 at RT. We cannot exclude that this hopping is tip-induced. In the case of a system where the atom jumps between two equivalent positions, the tip could be positioned above one of the positions and current oscillations could be measured. A telegraphic signal should be obtained from which one might determine the activation barrier for the jumps. However, due to the thermal drift we were unable to perform this experiment.

At room temperatures, only one type of the In dimer is observed, the so called *inter-dimer*. It is formed by two In adatoms bonded to adjacent Si dimer rows. However, another In dimer was reported by ab-initio calculations [69], called *intra-dimer*. It is energetically less favourable than the inter-dimer by 0.24 eV. Intra-dimer atoms sit on the top of a single Si dimer row (see Fig. 32). Similar dimers are also predicted for Al [62]. Fig. 32 shows 0.1 ML of In at 77 K. Both inter- and intra- dimers are present on the surface, with approximately 1:1 ratio. The relative height of the intra-dimer (≈ 3.5 Å) is more than can be explained by morphology (In-Si bond length is 2.76 Å [69]) and suggests existence of hybridized $s + p_z$ -orbitals protruding away from the surface similarly as for the chain termination by a single atom. Radny [69] reports the intra-dimers to be metallic and the In-In coupling fully occupied (compared to half-filled for inter-dimer). However, the LT

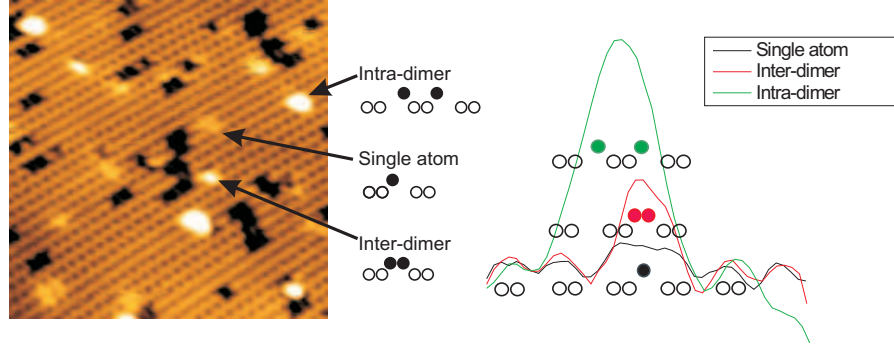


Figure 32: Left: Both types of In dimer are present on Si(100) at 85 K (deposited at 30 K). Right: Line profiles of the object indicated by arrows. Note the large height difference between inter- and intra- dimer.

STS measurements were not taken due to difficulties with drift correction at very low temperatures. Further detailed results of the diffusion measurements will be published in a doctoral thesis by Martin Setvin.

7 Summary

This thesis deals with the growth and evolution of indium chains on the Si(100)- 2×2 . Both the experimental data and results from kinetic Monte Carlo simulations are presented.

We observed directly the growth and decay of the In chains at room temperature and identified the chain termination by a single atom, dimer and C-defect. This lead to formulation of a growth model: the chains grow and decay in steps by a single atom. Chain end terminated by a single atom is significantly less stable (detachment frequency at RT $f = 0.25$ Hz) compared to the dimer-termination ($f = 0.08$ Hz). C-defects were identified as primary nucleation centres for growth of the chains. In the relaxed state, around 70 - 90% of the chains are terminated with a C-defect. We determined the energy barriers for the detachment of In atoms from the chains, including the exponential prefactor. The barriers are:

| | E_{det} (eV) | prefactor ν_0 (Hz) |
|-------|----------------|--------------------------|
| CD+3 | 0.82 ± 0.01 | $8.7\times 10^{13\pm 2}$ |
| CD+2n | 0.87 ± 0.02 | $6.5\times 10^{13\pm 1}$ |

Note that the value of the exponential prefactor is often used in many models for the Si(100), but so far has never been directly measured. The measured value is in agreement with the generally used value of 1×10^{13} Hz and justifies its use.

Based on the physical model and the obtained detachment energies we programmed a KMC simulation and fitted diffusion barriers as the variable parameter. The results indicate that the diffusion of In on the anisotropic 2×1 reconstruction is almost isotropic ($E_{\parallel} = 0.63$ eV; $E_{\perp} = 0.65$ eV). The diffusion barriers obtained from our simulations are much higher than values obtained from ab-initio calculations (≈ 0.27 eV) and our preliminary results from the low temperature direct observations (≈ 0.3 eV). While ab-initio and direct observation values are truly local energy barriers between neighboring two minima in the potential surface, the simulation-based value is rather an "effective" value incorporating effects such as limiting diffusion due to chains and temporary adatom trapping at missing dimer defects or step edges.

Several factors may be responsible for the higher obtained diffusion barriers. Diffusion could be blocked at step edges, but in our experiments we selected large terraces to mitigate this effect and furthermore, due to presence of other In chains and C-defects the free atoms are less likely to run into a step edge. Low-temperature experiments indicate that the In atoms are trapped at the missing dimer defects, though contrary to trapping at the C-defects, atoms have been

observed to jump away from a missing dimer. This trapping can cause higher effective diffusion barrier. The diffusion pathes are more complicated in reality than those considered by the model. The forbidden zones introduced in our model block atom hopping and may even cause some areas, surrounded by In chains, to be inaccessible. It has been observed that atoms can actually migrate into/ out of such areas. Our model should be modified to reflect this, perhaps by not fully prohibiting atoms from entering the forbidden zones, but only by assigning such events small probabilities.

The simulations also explain the unexpected monotonically decreasing shape of the island size distribution. The reason is the decay of chains when the released atoms nucleate in new chains. The simulations also confirmed the relationship between the concentrations of C-defects and the average chain length. In any future applications of the chains, attention must be paid to the partial pressure of water in the chamber. The monotonically decreasing shape of the distribution function also means, that the system is close to the thermal equilibrium. In the thermal equilibrium, the shape of the distribution function is no longer dependent on kinetic parameters such as diffusion barriers. So, the proximity of the system to thermal equilibrium lowers the accuracy of the diffusion barriers obtained from the KMC simulations. A general solution to this problem is to prevent the system from reaching the equilibrium. At temperatures below 200 K, detachment of atoms from chains is effectively stopped and the system frozen. Then, its state depends on the kinetics of processes occurring during the growth.

Low temperature experiments brought first-ever observation of a single free group III metal atom on the Si(100) surface, as well as of the predicted intra-dimer. The observed adsorption position confirms theoretical prediction. Flip-flop hopping of the adatom between the two equivalent positions in the Si-dimer row was observed at 85 K. The adatom hopping depends on the substrate reconstruction ($c(4\times 2)$ or $p(2\times 2)$). We observed that it is impossible to image single In adatoms at LT in empty states, as this causes an immediate tip crash. We attribute this effect to attractive electrostatic force between the tip and the positively charged In. Further results of the LT studies will be published in doctoral thesis by Mr. Martin Setvin.

References

- [1] D. J. Wales *Science*, vol. 271, p. 925, 1996.
- [2] M. Ceriotti, R. Fernando, and F. Montalenti *Nanotechnology*, vol. 17, p. 3556, 2006.
- [3] J. Schwoebel *J. of Appl. Sci*, vol. 37, p. 3682, 1996.
- [4] J. A. Venables *Introduction to Surface and Thin Film Processes*, vol. Cambridge University Press, pp. 150–154, 2000.
- [5] M. Bartelt and J. W. Evans *Phys. Rev. B*, vol. 46, p. 12675, 1992.
- [6] J. W. Evans and M. C. Bartelt *J. Vac. Sci. Technol. A*, vol. A12, p. 1800, 1994.
- [7] C. Ratsch and J. A. Venables *J. Vac. Sci. Tech.*, vol. A21, pp. S96–S109, 2003.
- [8] V.I.Tokar and H. Dreysee *Phys. Rev. B*, vol. 74, p. 115414, 2006.
- [9] M. Albao, M. Evans, J. Nogami, D. Zorn, M. Gordon, and J. Evans *Phys. Rev. B*, vol. 72, p. 035426, 2005.
- [10] P. Hohenberg and W. Kohn *Phys. Rev.*, vol. 136B, p. 864, 1964.
- [11] W. Kohn and L. J. Sham *Phys. Rev.*, vol. 140A, p. 1133, 1965.
- [12] A. B. B. and M. H. Kalos and J. L. Lebowitz *J. Comput. Phys.*, vol. 17, p. 10, 1974.
- [13] P. A. Maksym *Semicond. Sci. Technol.*, vol. 3, p. 594, 1988.
- [14] S. Clarke, M. R. Wilby, and D. D. Vvedensky *Surf. Sci.*, vol. 225, p. 91, 1991.
- [15] M. Jaraiz, E. Rubio, P. Castrillo, I. Pelaz, L. Bailon, J. Barbolla, G. H. Gilner, and C. S. Rafferty *Mat. Sci. in Sem. Proc.*, vol. 3, p. 59, 2000.
- [16] J. Tersoff *Phys. Rev. B*, vol. 32, p. 6968, 1985.
- [17] J. Tersoff and D. R. Hamann *Phys. Rev. Lett*, vol. 50, p. 1998, 1983.
- [18] C. J. Chen *Introduction to Scanning Tunneling Microscopy*, vol. Oxford University Press, 1993.

- [19] R. Wiesendanger *Cambridge University Press*, vol. Scanning Probe Microscopy and Spectroscopy: Methods and Applications, 1994.
- [20] L. Petersen, M. Schunack, B. Schaefer, and et.al *Rev. Sci. Inst.*, vol. 72, p. 1438, 2001.
- [21] E. Ganz, S. K. Theiss, I. Hwang, and J. Golovchenko *Phys. Rev. Lett.*, vol. 68, p. 1567, 1992.
- [22] J. M. Gomez-Rodriguez, J. Y. Veuillen, and R. C. Cinti *J. Vacuum Science & Technology B*, vol. 14, pp. 1005–1009, 1996.
- [23] Z. Y. Zhang, F. Wu, H. J. W. Zandvliet, B. Poelsema, H. Metiu, and M. G. Lagally *Phys. Rev. Lett.*, vol. 74, pp. 3644–3647, 1995.
- [24] N. Kitamura, M. G. Legally, and M. B. Webb *Phys. Rev. Lett.*, vol. 71, p. 2082, 1993.
- [25] P. Sobotík, P. Kocán, and I. Ošťádal *Surf. Sci.*, vol. 537, no. 1-3, p. 442, 2003.
- [26] X. C. Guo and R. J. Madix *Surf. Science*, vol. 550, pp. 81–92, 2004.
- [27] X. C. Guo and R. J. Madix *Accounts Chem. Research*, vol. 36, pp. 471–480, 2003.
- [28] W. Jun, C. E. J. Mitchell, R. G. Egdell, and J. S. Foord *Surf. Science*, vol. 506, pp. 66–79, 2002.
- [29] X. C. Guo and R. J. Madix *Surf. Science*, vol. 501, pp. 37–48, 2002.
- [30] S. Hildebrandt, C. Hagendorf, T. Doege, C. Jeckstiess, R. Kulla, H. Neddermeyer, and T. Uttich *J. Vacuum Science & Technology A-vacuum Surfaces Films*, vol. 18, pp. 1010–1015, 2000.
- [31] H. Norenberg and G. A. D. Briggs *Microscopy Semiconducting Materials 1999, Proc.*, pp. 637–640, 1999.
- [32] P. Sobotik, I. Ostadal, and P. Kocan *Surf. Sci. Lett*, vol. 537, p. L442, 2003.
- [33] B. S. Schwarzenruber *Phys. Rev. Lett*, vol. 76, p. 459, 1996.
- [34] M. Setvin and J. Javorsky *Studium vlivu procesu pri autoemisi na vlastnosti wolframovych hrotu pro STM - studentsky projekt*, vol. MFF UK - KEVF, 2005.

- [35] P. Kocan *Studium epitaxneho rstu na rekonstruovanych povrch Si*, vol. MFF UK - KEVF, 2004.
- [36] T. T. Tsong, “A historic perspective of fim and stm studies of surface diffusion,” *Mat. Sci. Eng. A*, vol. 353, p. 1, 2003.
- [37] R. M. Feenstra and S. Gaan *Phys. Rev. B*, vol. 71, p. 125316, 2005.
- [38] D. M. Eigler and E. K. Schweizer, “Positioning single atoms with a scanning tunneling microscope,” *Nature*, vol. 344, p. 524, 1990.
- [39] S. W. Hla, K. F. Braun, and K. H. Rieder *Phys. Rev. B*, vol. 67, 2003.
- [40] D. Fujita and T. Kumakura *Appl. Phys. Lett.*, vol. 82, p. 2329, 2003.
- [41] A. Houel, D. Tonneau, N. Bonnail, H. Dallaporta, and V. I. Safarov *J. Vac. Sci. Technol. B*, vol. 20, p. 2337, 2002.
- [42] R. Hamers, R. Tromp, and J. Demuth *Phys. Rev. B*, vol. 34, p. 5343, 1986.
- [43] D. Chadi *Phys. Rev. Lett.*, vol. 43, pp. 43–47, 1979.
- [44] A. Ramstad, G. Brocks, and P. Kelly *Phys. Rev. B*, vol. 51, p. 14504, 1995.
- [45] P. Sobotik and I. Ostadal *Surf. Sci.*, vol. 602, p. 2835, 2008.
- [46] M. Ono, A. Kamoshida, N. Matsuura, T. Eguchi, and Y. Hasegawa *Physica B*, vol. 329, p. 1644, 2003.
- [47] T. Uda and et al. *Progr. Surf. Sci.*, vol. 76, p. 147, 2004.
- [48] Y. J. Li, H. Nomura, and N. O. et. al. *Phys. Rev. Lett.*, vol. 96, p. 106104, 2006.
- [49] M. Dubois, L. Perdigo, C. Delerue, and et. al. *Phys. Rev. B.*, vol. 71, p. 165322, 2005.
- [50] J. E. Northrup *Phys. Rev. B*, vol. 47, p. 10032, 1993.
- [51] R. Hamers and U. Kohler *J. Vac.Sci.Technol.*, vol. A 7, p. 2854, 1989.
- [52] J. E. Northrup *Phys. Rev. B*, vol. 69, p. 085312, 12004.
- [53] M. Z. Hossain, Y. Yamashita, K. Mukai, and J. Yoshinobu *Phys. Rev. B*, vol. 67, p. 153307, 2003.

- [54] S. Okano and A. Oshiyama *Surf. Sci.*, vol. 554, p. 272, 2004.
- [55] J. Nogami, S.-I. Park, and C. Quate *Appl. Phys. Lett.*, vol. 53, p. 2086, 1988.
- [56] J. Nogami, A. Baski, and C. Quate *Phys. Rev. B*, vol. 44, p. 1415, 1991.
- [57] T. C. Shen, C. Wang, and J. R. Tucker *Phys. Rev. Lett.*, vol. 78, p. 1271, 1997.
- [58] A. Baski, J. Nogami, and C. Quate *J. Vac. Sci. Tech*, vol. A9, p. 1946, 1991.
- [59] J. Nogami, A. Baski, and C. Quate *Phys. Rev. B*, vol. 43, p. 9316, 1991.
- [60] X. Q. Dai and W.-W. J. et.al *Surf. Sci.*, vol. 77, p. 572, 2004.
- [61] Y. Umeno and T. Kitamura *Modell. Simul. Mater. Sci. Eng.*, vol. 12, p. 1147, 2004.
- [62] G. Brocks *Phys. Rev. Lett.*, vol. 70, p. 2786, 1993.
- [63] Z. C. Dong, D. Fujita, and H. Nejoh *Phys. Rev. B*, vol. 63, p. 115402, 2001.
- [64] P. Kocan, P. Sobotik, I. Ostadal, J. Javorsky, and M. Setvin *Surf. Sci.*, vol. 601, p. 4506, 2007.
- [65] A. A. Baski, J. Nogami, and C. F. Quate *Phys. Rev. B*, vol. 44, p. 11167, 1991.
- [66] L. Li, C. Koziol, K. Wurm, Y. Hong, and et.al. *Phys. Rev. B*, vol. 50, p. 10834, 1994.
- [67] L. Jure and et.al. *Appl. Surf. Sci.*, vol. 162-163, p. 638, 2000.
- [68] J. Pudl *Thesis*, vol. In progress, 2010.
- [69] M.W.Radny, P. Smith, and L. Jurczyszyn *Phys. Rev. B*, vol. 81, p. 085424, 2010.
- [70] M. Evans and J. Nogami *Phys. Rev. B*, vol. 59, p. 7644, 1999.
- [71] I. Ostadal, J. Javorsky, P. Kocan, P. Sobotik, and M. Setvin *J. Phys. Conf. Ser.*, vol. 100, p. 2006, 2008.
- [72] Z. C. Dong and et.al *Ultramicroscopy*, vol. 73, pp. 169–174, 1998.

- [73] P. Kocan, L. Jurczyszyn, P. Sobotik, and I. Ostadal *Phys. Rev. B*, vol. 77, p. 113301, 2008.
- [74] M. Albao, C.-C. Hsu, D. B. Putungan, and F.-C. Chuang *Surf. Sci*, vol. 604, p. 396, 2010.
- [75] M. A. Albao, J. W. Evans, and F.-C. Chuang *J. Phys. Condens. Matter*, vol. 21, p. 405002, 2009.
- [76] H.-M. Tutuncu and S. D. et al. *Physical Review B*, vol. 72, p. 085327, 2005.
- [77] N. Takagi, S. Shimonaka, T. Aruga, and M. Nishijima *Physical Review B*, vol. 60, p. 10919, 1999.
- [78] G. Dolling and R. A. Cowley *Proc. Phys. Soc*, vol. 88, p. 463, 1966.